NISSUNA UMANA INVESTIGAZIONE SI PUO DIMANDARE VERA SCIENZIA
S'ESSA NON PASSA PER LE MATEMATICHE DIMOSTRAZIONI
LEONARDO DA VINCI

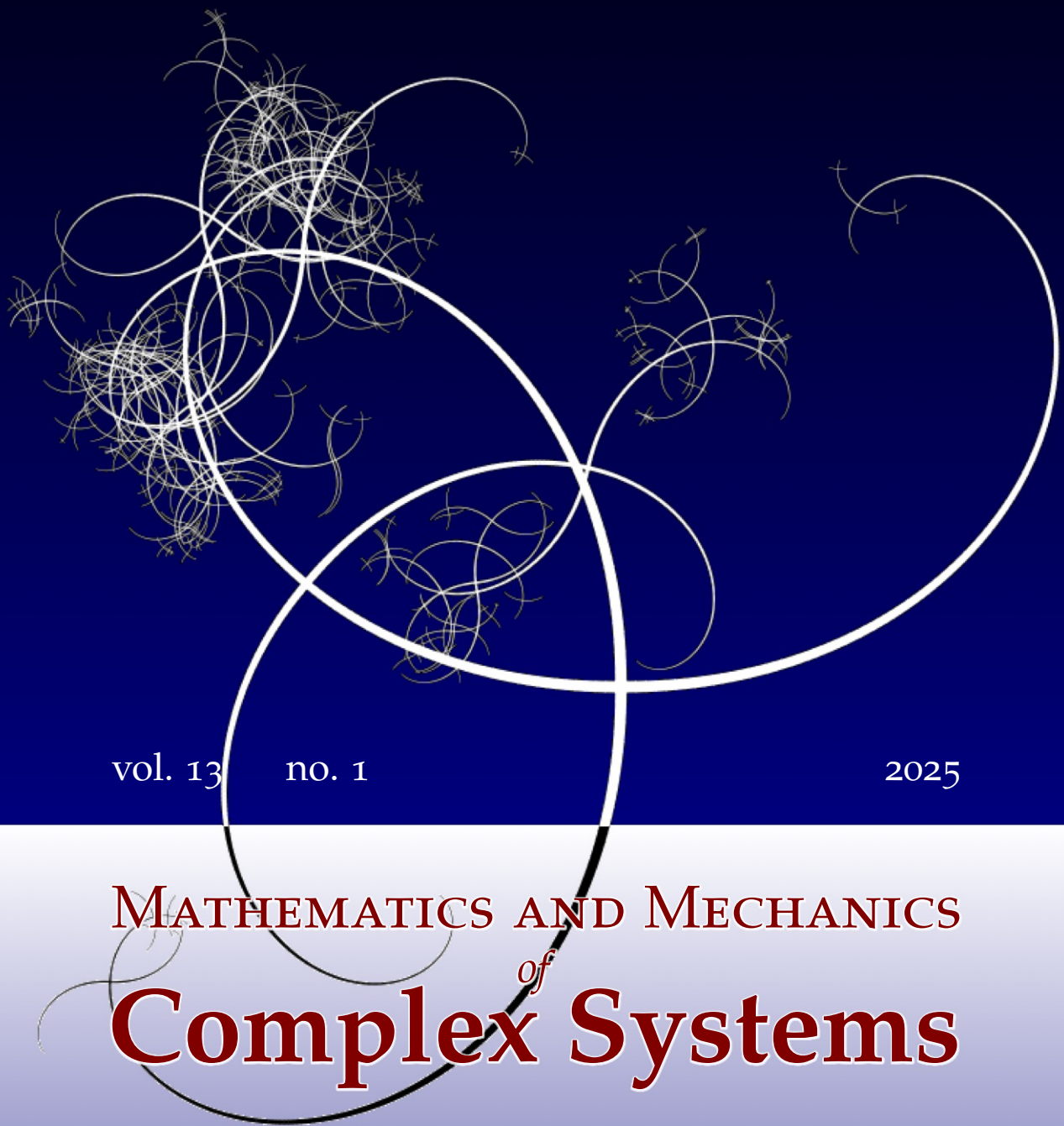

vol. 13 no. 1 2025

Mathematics and Mechanics *of* Complex Systems

Nurettin Yilmaz, Luca Placidi, Anil Misra and Francesco Fabbrocino

A PARAMETRIC STUDY ON A GRANULAR MICROMECHANICS CONTINUUM-BASED HEMIVARIATIONAL APPROACH: UNRAVELING THE EMERGENCE OF CRITICAL STATES IN GRANULAR MATERIALS

msp

MATHEMATICS AND MECHANICS OF COMPLEX SYSTEMS
Vol. 13 (2025), No. 1, pp. 25–54
DOI: 10.2140/memocs.2025.13.25

A PARAMETRIC STUDY ON A GRANULAR MICROMECHANICS CONTINUUM-BASED HEMIVARIATIONAL APPROACH: UNRAVELING THE EMERGENCE OF CRITICAL STATES IN GRANULAR MATERIALS

NURETTIN YILMAZ, LUCA PLACIDI, ANIL MISRA AND FRANCESCO FABBROCINO

A numerical model was established in earlier work to investigate the macroscale critical state, which determines the mechanical behavior of sheared granular materials. This paper explores the behavior of this model by conducting a parametric study that varies the constitutive parameters over a wide range. This study is essential to define the combination of material parameters that will lead to the emergence of critical state along the classical response. According to the typical critical state behavior, while the material volume and stress remain unchanged under large shear deformation, the material continues to deform. The critical state concept is examined using a granular micromechanics approach within a numerical framework. In this model, elastic and dissipation energies for a generic grain-pair interaction are adapted using a hemivariational principle. Karush–Kuhn–Tucker-type conditions are derived through a hemivariational principle, providing evolution equations for damage and plastic irreversible phenomena. The coupled damage and plasticity, which are crucial for material strength properties, are associated with grain-pair contact loss and irreversible deformation. Notably, damage-elastoplastic spring elements are described in order to link the micro and macro mechanisms, using orientationally based grain-pair interactions, decomposed into normal and tangential directions. The material properties of specimens with different initial density states are adapted according to dilatancy/compaction characteristics to achieve the idealized critical state behavior. The present model is then applied to simulate the stress and volumetric strain behaviors under varying characteristic compression constitutive parameters.

1. Introduction

Granular media consists of assembly of such frictional materials related to interactions between particles under external loads, which are affected by the lack of strong bonding forces, leading to sliding of grains. In the establishment of this study, we aim to investigate the behavior of numerical model constructed to replicate the emergence of critical state for selected appropriate simulation parameters. the assessed particles in the model do not stick to each other (or have only a slight tendency) under the external mechanical loads, and particle interactions are adapted by experiencing compression and shear. These frictional materials attract a great deal of interest in various areas of science and engineering, such as the identification of deformation mechanisms in geomechanics, geotechnical engineering, and the

Communicated by Emilio Barchiesi.
Yilmaz is the corresponding author.
MSC2020: 74-10.
Keywords: critical state, parameter identification, hemivariational approach, Karush–Kuhn–Tucker conditions, damage and plasticity mechanics.

metallurgical and material industries. When the critical state is reached, which is a preferred concept in exploring the behavior of granular materials, the material volume and stress do not change under significant angular deformation. Wood [82] has presented one of the early studies on this phenomenon and examined the critical state on granular materials under triaxial compression and simple shear loadings. Theocharis et al. [77; 78] have discussed the necessity of additional microstructural conditions to maintain the critical state based on the performed discrete element method (DEM) experiment results. Since some challenges are addressed by directly investigating microstructural measurements through experiments, the anisotropic behavior of granular material can be achieved not only by following the arrangement of particles and the grain and surface contact mechanisms but also by completing a number of numerical simulations depending on various assumptions, as introduced by Pan et al. [59].

Computational models are powerful tools for revealing the mechanical behavior of materials in diverse environments. These models efficiently provide innovative solutions for structures and unique insights in the design of industrial processes. With the popularization of computational methods, modeling and simulating of granular materials become an interesting topic to observe their complex material characteristics. In terms of the convenience of modeling approaches, while a discrete description is widely applied in investigating the mechanical behavior of granular media (studies of discrete modeling include [17; 52; 74; 81]), continuum modeling is also useful in studying the mechanical characteristics of granular materials (see [21; 20; 47; 61]). Recent novel numerical methods involving coupling strategies, such as discrete-continuum approaches [53; 58; 57; 75; 84], draw attention to the exploration of granular materials from the mechanistic viewpoint. As the numerical solutions of such complex structures are usually time-consuming and may suffer from numerical instabilities, the progress of numerical models and approaches plays an important role.

To investigate the behavior of the critical state in granular materials, which is an essential concept, numerous efforts have been carried through the discrete element method (DEM) in the literature. DEM provides a thorough examination of individual particle interactions in relation to contact forces, displacements, and rotations. DEM simulations introduce predictions by adjusting the attributes of each particle in the random granular bulk, such as size, shape, and stiffness, based on experimental observations. Additionally, DEM can enhance understanding of the material's microstructure through grain-grain interactions (e.g., modification in coordination number and fabric anisotropy) while addressing macroscale behavior. Grain-level interactions in DEM can increase computational complexity and cost due to the vast number of particles in bulk materials. Furthermore, in 2D and 3D efforts of the critical state, deficiencies may arise during information transfer because of the varying properties of all grains. When the representative volume element is large enough, contact behavior in particles, such as idealized contact laws and simplified particle shapes (e.g., spheres or ellipsoids), can lead to unrealistic results and inaccuracies in simulations compared to real granular materials. DEM simulations express various grain characteristics, including the formation and evolution of force chains, initial packing density, fabric anisotropy, and particle breakage and fragmentation within the granular assembly, thereby affecting the critical state. Rothenburg and Kruyt [69] introduced a micromechanical theory of critical state

based plastic deformation in granular assemblies in relation to the disintegration of interparticle contacts, utilizing 2D discrete element simulations to unravel the evolution of the coordination number under shear deformations. Fabric evolution at the critical state has been employed for determining the anisotropy in contact orientations, eventually reaching a characteristic state (see for instance [50; 56]). Zhu et al. [90] investigated the critical state fabric of granular material in distinct failure modes and used mesoscale force-chains and mesoloops characteristics to explain that both localized and diffuse failure modes serve the same fabric. Drawing upon this initial research, Deng et al. [28] expanded the critical state beyond specific failure modes defining through a single proportional strain test across diverse loading scenarios. While it is emphasized that simulating granular materials using DEM can be challenging considering particle geometry, surface characteristics, and computational challenges, the micromechanical insights gained from DEM simulations refine continuum models. For example, Misra and Poorsolhjouy [51] provided informative work for identifying the macroscale characteristics using granular micromechanics in relation to the microscale stiffness coefficients. The role of fabric evolution adapting DEM within elastoplastic constitutive model was examined to unravel the anisotropic behavior of granular materials at critical state (see discrete element simulation results in [46; 37]).

The structural components with multifaceted interactions that constitute the complex material are defined utilizing continuum modeling approaches. Continuum modeling techniques, which are the constitutive models and the numerical methods within the critical state concept, have been implemented to predict the behavior of soils under various loading paths. In this regard, the finite element model (FEM)-based conventional elastoplastic frameworks, such as Cam-clay and the unified clay and sand, have been introduced as two types of critical state models by Sheng et al. [73]. The plasticity-based constitutive models, which have recently advanced under various loading paths by incorporating critical state concepts, have developed a hypoplastic framework without relying on traditional yield surfaces, plastic potential, flow, and hardening rules [83] and analyzed gravelly soil-structure interfaces using an elastoplastic model based on two-surface plasticity theory [70]. Alternatively, the role of fabric on the characterization of sand plasticity theory at critical state has been revealed by describing the anisotropic behavior of sand [46; 37; 60]. An integration of critical state concepts based on continuum description has been made along with the micromechanical elastoplasticity model (see the existing microstructural simulations [12; 44; 89]).

Variational methods are a fundamental framework for deriving the governing equations for various physical systems (see [10; 18; 19; 26]). Dell'Isola and Misra [23] discussed the principle of virtual work, which is a powerful tool that enables an effective micro-macro identification process and introduces the homogenization schema to explore exotic and innovative metamaterials. Variational techniques are vital for appropriately modeling and unraveling the complex mechanical properties of metamaterials (see [32] for the nonlinear wave dynamics of tensegrity metamaterials, [49] for dynamic analysis of periodic material structures, and [36; 41; 43] for composite materials), as these approaches take into account not just conventional cases but also dissipative processes (work on dissipative systems includes [16; 33; 86; 3]). Strain-gradient theory [4; 31; 87] and higher-gradient theory [1; 5; 2; 42; 72] extend classical continuum

mechanics to examine microstructural properties, employing variational principles. These approaches offer a way of affirming the strain-gradient constitutive parameters for mechanical metamaterials that exhibit nonidentical behaviors (see [6; 22]). In particular, an asymptotic homogenization technique was used in [71] to determine the metamaterial constitutive parameters by linking micro- and macroscale characteristics via strain gradient theory, and in [85] by solving a boundary value problem with FEM. Innovative experimental-numerical methodologies have been proposed to predict material characteristics by incorporating experimental tests and numerical simulations using neural networks [15; 34; 68], or a combination of digital image analysis and FEM simulation [9; 11; 35]. Ramaglia et al. [66; 67] conducted numerical investigations focusing on the understanding and effectiveness of fiber-reinforced strengthening strategies for masonry structures. Continuum models treat materials as continuous media; studies focusing on the prediction of the macroscopic behavior of pantographic metamaterials include [7; 14; 25; 27; 29; 38; 76].

The continuum framework for granular materials simplifies complex particle interactions and provides a well-developed theoretical method, leveraging practical approaches to describe macroscopic properties such as stress, strain, and density. In parallel, the granular micromechanics approach (GMA) is designated to characterize the behavior of granular materials (see for instance [39; 40; 54; 55]). To this end, the establishment of continuum models for granular materials addressing the effective grain-pair interactions is based on a GMA. The continuum description is kinematically associated with granular micromechanics via Piola's ansatz (for homogenizing micro-models for metamaterials see [24; 80]). By considering effective grain-scale relationships, a GMA exposes the average macroscale behaviors by integrating these interactions over all orientations. The continuum model established based on a GMA detects grain-pair and kinematic variables from the micro-macro relationship regarding the elastic and dissipation energy functionals. These effective energies are defined by damage-elastoplastic spring elements and explore grain-scale interactions in normal and tangential directions. Notably, the relative displacement component along the vector connecting the grains from their centroids is called the normal component while the perpendicular component to the grain-pair direction is defined as tangential. The homogenized energy functionals are adopted, and a hemivariational principle is then used to derive the Karush–Kuhn–Tucker (KKT) conditions via governing equations (see [79; 48; 63] for the application of a hemivariational principle). KKT conditions provide the evolution equations of damage and plasticity irreversible phenomena with regard to all grain-pair orientations. In granular micromechanics, damage is identified as the loss of stiffness, and plasticity is referred to as the cumulative irrecoverable grain-pair displacements. Numerical simulations have been successfully performed for both homogeneous and nonhomogeneous deformations using the present model [30; 48; 63; 64; 79].

The fundamental aspect of the work is to present a comprehensive parametric study on a numerical model utilizing a GMA to explore the combination of constitutive parameters affecting the critical state with respect to the classical way in granular materials. A parametric study can clarify the further refinements in predicting the macroscale behavior of granular materials, utilizing a numerical model to better capture experimental findings. In light of the following a parametric study, the preliminary efforts are expanded

to gain insight into determining both energy equations and simulation parameters to strengthen the ability of numerical model predictions under different loading histories. Alternatively, a systematic approach replicates the experimental results by characterizing higher accuracy, consistency, and confidence with validating and calibrating continuum model findings. For instance, the advanced numerical techniques are employed to simulate the deformation behavior of UHP-FRC (ultra-high performance fiber-reinforced concrete) by introducing the new constitutive parameters through experimental results (see the recent work of Placidi et al. [65]). To investigate the emergence of critical state, we transferred a novel dissipation energy to observe the desired evolution damage and plasticity coupling, renewing the dissipation energy used in [62]. Yilmaz et al. [88] presented a developed and validated continuum model to examine the critical state concept by comparing the numerical predictions with experimental observations qualitatively. In this work, we attain three different specimens, namely dense, mid-dense, and loose, with different initial void ratios, and only homogeneous deformations are examined. It is noteworthy that a parametric study includes the optimization process thanks to a deeper understanding of parameter changes how influences the overall behavior of the material. By systematically varying the constitutive parameters, the new material properties are integrated into the model, affecting both the strength characteristics and the evolution of damage and plasticity. This work not only improves our understanding of the continuum framework based on the investigation of granular material behavior, but also establishes the refinements of effectively formulated elastic and dissipation energy functionals to replicate more accurate and reliable results in the future.

This paper is organized as follows. Section 2 presents the homogenized energy terms based on a single grain-grain interaction to derive the governing equations and the threshold equations for the coupled damage and plastic phenomena by utilizing a hemivariational principle. Section 3 reports simulations for all specimens with different initial density states to investigate the emergence of critical state and provided with regard to the parametric studies to elucidate the effects of simulation parameters. Section 4 summarizes the findings and discusses implications for future works.

2. Mathematical model

2.1. ***Elastic energy.*** In this continuum framework, we use the damage-elastoplastic spring elements describing the grain-pair interactions for each orientation and a given point $\boldsymbol{X}$ of the continuum body $\mathcal{B}$, characterized by the unit vector $\hat{\boldsymbol{c}} = \cos\theta\,\hat{\boldsymbol{e}}_1 + \sin\theta\,\hat{\boldsymbol{e}}_2$, defined with respect to the polar representation depending on the orientation, $\theta \in [0, 2\pi]$, in an orthonormal frame of reference $(O, \hat{\boldsymbol{e}}_1, \hat{\boldsymbol{e}}_2)$. An elastic energy is correlated for each grain-pair interaction over all orientations, regarding the unit circle $\mathcal{S}$ in 2D model. We have an elastic energy density U in the continuum description obtained with the homogenization rule, following Barchiesi et al. [8]:

$$U = \int_{\mathcal{S}} \left(\tfrac{1}{2} k_{\eta,D} (u_\eta^{\mathrm{el}})^2 + \tfrac{1}{2} k_{\tau,D} (u_\tau)^2\right) dA, \tag{1}$$

where dA is the area portion around the unit circle $\mathcal{S}$, and the elastic normal displacement u_η^{el} is found by

the difference between the normal displacement u_η and the plastic normal displacement u_η^{pl}:

$$u_\eta^{\mathrm{el}} = u_\eta - u_\eta^{\mathrm{pl}}, \tag{2}$$

where the plastic normal displacement u_η^{pl} is the difference between two plastic multipliers referring to the tension λ_η^t and compression λ_η^c plastic variables:

$$u_\eta^{\mathrm{pl}} = \lambda_\eta^t - \lambda_\eta^c. \tag{3}$$

The normal displacement (a scalar quantity), its square and the square of the norm of the tangent displacement vector ($u_\tau = \sqrt{u_{\tau_i} u_{\tau_i}}$) are obtained in terms of intergranular distance L and the strain $\boldsymbol{G}$:

$$u_\eta = L G_{ij} \hat{c}_i \hat{c}_j, \tag{4}$$

$$(u_\eta)^2 = L^2 G_{ij} G_{ab} \hat{c}_i \hat{c}_j \hat{c}_a \hat{c}_b, \tag{5}$$

$$(u_\tau)^2 = 4L^2 G_{ij} G_{ab} (\delta_{ia} \hat{c}_j \hat{c}_b - \hat{c}_i \hat{c}_j \hat{c}_a \hat{c}_b); \tag{6}$$

here

$$\boldsymbol{G} = \tfrac{1}{2}(\boldsymbol{F}^{\mathrm{T}} \boldsymbol{F} - \boldsymbol{I}), \tag{7}$$

is the Green–St. Venant tensor, expressed in terms of $\boldsymbol{F} = \nabla \boldsymbol{\chi}\big|_{\boldsymbol{X}}$, where $\boldsymbol{\chi}(\boldsymbol{X}, t)$ is the placement function which in $\boldsymbol{X}$ and t represent the position and time. The damaged $k_{\eta,D}$ normal stiffness is expressed by

$$k_{\eta,D} = k_{\eta,D}^t \Theta(u_\eta^{\mathrm{el}}) + k_{\eta,D}^c \Theta(-u_\eta^{\mathrm{el}}), \tag{8}$$

where the damaged tension $k_{\eta,D}^t$ and compression $k_{\eta,D}^c$ normal stiffness and the damaged tangent $k_{\tau,D}$ stiffness are described in terms of the normal and tangential damage variables, D_η and D_τ, as follows:

$$k_{\eta,D}^t = k_\eta^t (1 - D_\eta), \quad k_{\eta,D}^c = k_\eta^c (1 - D_\eta), \quad k_{\tau,D} = k_\tau (1 - D_\tau). \tag{9}$$

Besides, k_η^t, k_η^c, and k_τ represent the nondamaged normal stiffness in tension and compression, respectively, and the nondamaged tangential stiffness. In the cases of tension and compression, the normal stiffness k_η differs and is expressed in terms of the Heaviside function $\Theta(x)$ (taking the value 1 if $x \geq 0$ and 0 otherwise) by

$$\Theta(x) = \frac{1}{2} + \frac{1}{\pi} \arctan \frac{x}{\alpha}, \tag{10}$$

where α is the regularization parameter, whose value should be much smaller than u_η^{el} in the numerical simulations. The normal displacement u_η is partitioned into elastic and plastic parts, and the square of its elastic part is calculated by inserting (4) into (2):

$$(u_\eta^{\mathrm{el}})^2 = (u_\eta - u_\eta^{\mathrm{pl}})^2 = L^2 G_{ij} G_{ab} \hat{c}_i \hat{c}_j \hat{c}_a \hat{c}_b - 2L u_\eta^{\mathrm{pl}} G_{ij} \hat{c}_i \hat{c}_j + (u_\eta^{\mathrm{pl}})^2. \tag{11}$$

Here we only consider homogeneous deformation, so the gradient of the Green–St. Venant tensor vanishes in (4), (5), and (11) ($G_{ij,h} = 0$). The homogenized continuum elastic energy density was first introduced

in (1) and can be written with respect to (6) and (11) as

$$U = \tfrac{1}{2}\mathbb{C}_{ijab}G_{ij}G_{ab} + \mathbb{P}_{ij}G_{ij}, \tag{12}$$

where the elastic stiffness tensors $\mathbb{C}_{ijab}$ and $\mathbb{P}_{ij}$ are expressed by

$$\begin{aligned}\mathbb{C}_{ijab} = L^2 \int_{\mathcal{S}} k_\eta (1-D_\eta)\hat{c}_i\hat{c}_j\hat{c}_a\hat{c}_b \, dA \\ + L^2 \int_{\mathcal{S}} k_\tau (1-D_\tau)\big((\delta_{ia}\hat{c}_j\hat{c}_b + \delta_{ib}\hat{c}_j\hat{c}_a + \delta_{ja}\hat{c}_i\hat{c}_b + \delta_{jb}\hat{c}_i\hat{c}_a) - 4\hat{c}_i\hat{c}_j\hat{c}_a\hat{c}_b\big)\, dA,\end{aligned} \tag{13}$$

$$\mathbb{P}_{ij} = -L \int_{\mathcal{S}} k_\eta (1-D_\eta) u_\eta^{\mathrm{pl}} \hat{c}_i\hat{c}_j \, dA. \tag{14}$$

Overall, the second-order tensor $\mathbb{P}_{ij}$, called as prestress tensor, characterizes the normal plastic relative displacement component independently of the strain tensor $\boldsymbol{G}$. Interested readers may consult [25; 63], which delve into the adapted homogenization approach, for in-depth discussion.

2.2. ***Dissipation energy potential.*** We consider two dissipation phenomena as damage and plasticity in the proposed model. Damage indicates the cumulative effects arising from grain-scale mechanisms, and therefore introduces the collapse or buckling of particle chains and clusters due to particle rotation and rolling or grain sliding, and the loss of lateral support or confinement within the granular assembly. The proposed continuum model interprets damage as a loss of stiffness rather than the creation or loss of contacts between grains. Plasticity is characterized by the effective accumulation of irreversible deformations and essentially driven by grain-pair sliding and separation along with the considered orientations. Subsequently, these two coupled phenomena provide a comprehensive description of the rate-independent dissipative mechanisms governing the behavior of granular materials. Damage (D_η and D_τ) and plasticity (λ_η^t and λ_η^c) irreversible phenomena for a generic grain-pair are comprised into dissipation energy. The total dissipation energy potential W can be separated into two parts, corresponding to damage and plasticity:

$$W = W_D + W_{\mathrm{pl}}. \tag{15}$$

The term W_D splits as

$$W_D = W_D^\eta + W_D^\tau \tag{16}$$

into a normal part,

$$\begin{aligned}W_D^\eta = \frac{1}{2}k_\eta^c (B_\eta^c)^2 \Theta(-u_\eta^{\mathrm{el}})\Big[-D_\eta + \frac{2}{\pi}\tan\Big(\frac{\pi}{2}D_\eta\Big)\Big] \\ + \frac{1}{2}k_\eta^t (B_\eta^t)^2 \Theta(u_\eta^{\mathrm{el}})\big[2 + (D_\eta - 1)\big(2 - 2\log(1-D_\eta) + (\log(1-D_\eta))^2\big)\big],\end{aligned} \tag{17}$$

and a tangential one,

$$W_D^\tau = \tfrac{1}{2}k_\tau (B_\tau)^2\big[2 + (D_\tau - 1)\big(2 - 2\log(1-D_\tau) + (\log(1-D_\tau))^2\big)\big]; \tag{18}$$

here B_η^c and B_η^t are characteristic normal damage displacements associated with normal damage dissipation in compression and tension and B_τ is the characteristic tangent damage displacement related to the tangent

damage parameter. $B_\eta^t \ll B_\eta^c$ for lightly cohesive granular materials, damage rapidly evolves in tension as expected. Further, B_τ is expressed as

$$B_\tau = \tilde{B}_\tau(u_\eta^{\mathrm{el}}) = \frac{1}{2}(B_{\tau_0} + \alpha_1 B_{\tau_0}) + \frac{1}{\pi}(B_{\tau_0} - \alpha_1 B_{\tau_0}) \arctan \frac{u_\eta^{\mathrm{el}}}{\alpha}, \tag{19}$$

where α_1 is an additional constitutive parameter and arranges the quantities of B_τ with regard to tension and compression states. The dissipation energy potential obtained regarding plastic behavior is given by

$$W_{\mathrm{pl}} = (1 - D_\eta)\big(\sigma_\eta^t \lambda_\eta^t + \sigma_\eta^c \lambda_\eta^c + \sigma_{\eta\eta}^c (\lambda_\eta^c)^2\big), \tag{20}$$

where σ_η^t and σ_η^c serve the yielding parameters depending on tension and compression for the damage-elastoplastic behavior, and $\sigma_{\eta\eta}^c$ is the plastic hardening parameter. Here, we introduced a new dissipation energy potential for plasticity phenomenon to reach the classical critical state response; the dissipation energy W_{pl} in this model is different than in [48; 62; 79]. Note also that, in our approach, the energy formalism is the main ingredient of the model, and we can distinguish all terms being positive. The formalism does not explicitly enforce consistency with the second law of thermodynamics. From a mathematical perspective, the framework imposes no restrictions, and the total energy functional is a positive function. The elastic potential is defined as a quadratic function (see (1)) and positive definite. Dissipation potential can be distinguished into damage and plastic components. The damage dissipation potential W_D of (16)–(18) is always an increasing function with respect to damage and, because damage itself increases with time, W_D is also an increasing function of time. While the plastic dissipation potential W_{pl} (see (20)) is positive definite and zero at the initial state, W_{pl} does not consistently exhibit an increasing behavior. This characteristic arises from its dependence on $1 - D_\eta$, but maintains overall thermodynamic admissibility by remaining positive throughout the simulations.

2.3. ***Hemivariational principle for governing equations and Karush–Kuhn–Tucker conditions.*** The action functional of the system is expressed by the sum of elastic and dissipation energies,

$$\mathcal{E} = \int_{\mathcal{B}} U + W + \boldsymbol{b}^{\mathrm{ext}} \cdot \boldsymbol{u}\, d\Omega + \int_{\partial_{\boldsymbol{t}}\mathcal{B}} \boldsymbol{t}^{\mathrm{ext}} \cdot \boldsymbol{u}\, d\ell, \tag{21}$$

where $\boldsymbol{b}^{\mathrm{ext}}$ is the external distributed body force over the domain $\mathcal{B}$, and $\boldsymbol{t}^{\mathrm{ext}}$ is the external distributed force acting on the part $\partial_{\boldsymbol{t}}\mathcal{B}$ of the boundary $\partial\mathcal{B}$ on which we prescribe Neuman conditions. Here, let us consider $t_i \in \{t_i\}_{i=0,\dots,M}$, which is a monotonously increasing time range where $t_i \in \mathbb{R}$ and $M \in \mathbb{N}$. A displacement family $\boldsymbol{u}(\boldsymbol{X}, t_i)$ at each time $t = t_0, t_1, \dots, t_M$ is defined as a motion. The set AM_t of kinematically admissible displacements is determined, and the set AV_t, i.e., $\delta\boldsymbol{u}(\boldsymbol{X}, t_i) \in AV_t$, is determined as the associated space of kinematically admissible variations. Dirichlet boundary conditions on a part $\partial_{\boldsymbol{u}}\mathcal{B}$, of the boundary $\partial\mathcal{B}$ such that $\partial\mathcal{B} = \partial_{\boldsymbol{u}}\mathcal{B} \cup \partial_{\boldsymbol{t}}\mathcal{B}$ are implied with regard to the kinematically admissible displacement,

$$\boldsymbol{u} = \bar{\boldsymbol{u}} \qquad \forall\, \boldsymbol{X} \in \partial_{\boldsymbol{u}}\mathcal{B}. \tag{22}$$

Damage and plasticity are defined as irreversible kinematic quantities; thus their admissible variations are

always positive:

$$(\delta D_\eta, \delta D_\tau, \delta\lambda_\eta^t, \delta\lambda_\eta^c) \in \mathbb{R}^+ \times \mathbb{R}^+ \times \mathbb{R}^+ \times \mathbb{R}^+. \tag{23}$$

The first variation $\delta\mathcal{E}$ of the action functional defined in (21) is

$$\delta\mathcal{E} = \mathcal{E}(u_\eta+\delta u_\eta, u_{\tau_i}+\delta u_{\tau_i}, \lambda_\eta^t+\delta\lambda_\eta^t, \lambda_\eta^c+\delta\lambda_\eta^c, D_\eta+\delta D_\eta, D_\tau+\delta D_\tau) - \mathcal{E}(u_\eta, u_{\tau_i}, \lambda_\eta^t, \lambda_\eta^c, D_\eta, D_\tau). \tag{24}$$

The increment of the fundamental kinematic quantities, u_η, u_{τ_i}, D_η, D_τ, λ_η^t, and λ_η^c, are evaluated as the solution of the deformation process,

$$(\Delta u_\eta, \Delta u_{\tau_i}, \Delta\lambda_\eta^t, \Delta\lambda_\eta^c, \Delta D_\eta, \Delta D_\tau)_{t_i} = (u_\eta, u_{\tau_i}, \lambda_\eta^t, \lambda_\eta^c, D_\eta, D_\tau)_{t_i} - (u_\eta, u_{\tau_i}, \lambda_\eta^t, \lambda_\eta^c, D_\eta, D_\tau)_{t_{i-1}}, \tag{25}$$

where t_i and t_{i-1} represent the current and previous times. Thus, the increment $\Delta\mathcal{E}$ of total energy is used in the same manner:

$$\Delta\mathcal{E} = \mathcal{E}(u_\eta+\Delta u_\eta, u_{\tau_i}+\Delta u_{\tau_i}, \lambda_\eta^t+\Delta\lambda_\eta^t, \lambda_\eta^c+\Delta\lambda_\eta^c, D_\eta+\Delta D_\eta, D_\tau+\Delta D_\tau) - \mathcal{E}(u_\eta, u_{\tau_i}, \lambda_\eta^t, \lambda_\eta^c, D_\eta, D_\tau). \tag{26}$$

According to the definition in [79], the hemivariational principle is formulated as follows

$$\Delta\mathcal{E} \le \delta\mathcal{E} \quad \forall(\delta\boldsymbol{u}) \in AV_t, \qquad (\delta D_\eta, \delta D_\tau, \delta\lambda_\eta^t, \delta\lambda_\eta^c) \in \mathbb{R}^+ \times \mathbb{R}^+ \times \mathbb{R}^+ \times \mathbb{R}^+, \tag{27}$$

The governing equations, constitutive relations, and boundary conditions, respectively, are presented by applying a hemivariational approach along with the traditional variational approach,

$$\operatorname{div}(\mathbb{S}) + \boldsymbol{b}^{\text{ext}} = 0 \qquad \forall\, \boldsymbol{X} \in \mathcal{B}, \tag{28}$$

$$\mathbb{S} = \mathbb{C}\boldsymbol{G} + \mathbb{P} \qquad \forall\, \boldsymbol{X} \in \mathcal{B}, \tag{29}$$

$$\mathbb{S}\boldsymbol{n} = \boldsymbol{t}^{\text{ext}} \qquad \forall\, \boldsymbol{X} \in \partial_t\mathcal{B}, \tag{30}$$

where $\boldsymbol{n}$ is the outward unit normal vector to the domain boundary and $\mathbb{S}$ is the stress tensor giving the elastic energy per unit area in (12):

$$\mathbb{S}_{ij} = \frac{\partial U}{\partial G_{ij}} = \mathbb{C}_{ijab}G_{ab} + \mathbb{P}_{ij}. \tag{31}$$

Finally, Karush–Kuhn–Tucker (KKT) type conditions are derived corresponding to the four irreversible kinematic descriptors

$$\Big\{ -\tfrac{1}{2}k_\eta(u_\eta - \lambda_\eta^t + \lambda_\eta^c)^2 + \tfrac{1}{2}k_\eta^c(B_\eta^c)^2\Theta(-u_\eta^{\text{el}})\tan^2\Big(\frac{\pi}{2}D_\eta\Big) + \tfrac{1}{2}k_\eta^t(B_\eta^t)^2\Theta(u_\eta^{\text{el}})(\log(1-D_\eta))^2 - \sigma_\eta^t\lambda_\eta^t - \sigma_\eta^c\lambda_\eta^c - \sigma_{\eta\eta}^c(\lambda_\eta^c)^2\Big\}\Delta D_\eta = 0, \tag{32}$$

$$\Big\{ -\tfrac{1}{2}k_\tau(u_\tau^2) + \tfrac{1}{2}k_\tau(B_\tau)^2(\log(1-D_\tau))^2\Big\}\Delta D_\tau = 0, \tag{33}$$

$$\Big\{ -k_\eta(1-D_\eta)(u_\eta - \lambda_\eta^t + \lambda_\eta^c) + (1-D_\eta)\sigma_\eta^t\Big\}\Delta\lambda_\eta^t = 0, \tag{34}$$

$$\Big\{k_\eta(1-D_\eta)(u_\eta - \lambda_\eta^t + \lambda_\eta^c) + (1-D_\eta)(\sigma_\eta^c + 2\sigma_{\eta\eta}^c\lambda_\eta^c)\Big\}\Delta\lambda_\eta^c = 0. \tag{35}$$

A compact form for the KKT conditions is given by

$$\left\{D_\eta - \tilde{D}_\eta(u_\eta, \lambda_\eta^t, \lambda_\eta^c)\right\}\Delta D_\eta = 0, \tag{36}$$

$$\left\{D_\tau - \tilde{D}_\tau(u_\eta^{\mathrm{el}}, u_\tau)\right\}\Delta D_\tau = 0, \tag{37}$$

$$\left\{\lambda_\eta^t - \tilde{\lambda}_\eta^t(u_\eta, \lambda_\eta^c)\right\}\Delta \lambda_\eta^t = 0, \tag{38}$$

$$\left\{\lambda_\eta^c - \tilde{\lambda}_\eta^c(u_\eta, \lambda_\eta^t)\right\}\Delta \lambda_\eta^c = 0, \tag{39}$$

where the threshold functions $\tilde{D}_\eta$, $\tilde{D}_\tau$, $\tilde{\lambda}_\eta^t$, and $\tilde{\lambda}_\eta^c$ are given by

$$\tilde{D}_\eta(u_\eta, \lambda_\eta^t, \lambda_\eta^c) = \begin{cases} 1 - \exp\Big(-\dfrac{1}{B_\eta^t}\sqrt{\big(u_\eta - \lambda_\eta^t + \lambda_\eta^c\big)^2 + \dfrac{2}{k_\eta}\big(\sigma_\eta^t\lambda_\eta^t + \sigma_\eta^c\lambda_\eta^c + \sigma_{\eta\eta}^c(\lambda_\eta^c)^2\big)}\Big) \\ \qquad\qquad\qquad\qquad \text{if } u_\eta^{\mathrm{el}} = u_\eta - \lambda_\eta^t + \lambda_\eta^c \geq 0, \\ \dfrac{2}{\pi}\arctan\Big(\dfrac{1}{B_\eta^c}\sqrt{\big(u_\eta - \lambda_\eta^t + \lambda_\eta^c\big)^2 + \dfrac{2}{k_\eta}\big(\sigma_\eta^t\lambda_\eta^t + \sigma_\eta^c\lambda_\eta^c + \sigma_{\eta\eta}^c(\lambda_\eta^c)^2\big)}\Big) \\ \qquad\qquad\qquad\qquad \text{if } u_\eta^{\mathrm{el}} = u_\eta - \lambda_\eta^t + \lambda_\eta^c < 0, \end{cases} \tag{40}$$

$$\tilde{D}_\tau(u_\eta^{\mathrm{el}}, u_\tau) = 1 - \exp\left(-\frac{u_\tau}{\tilde{B}_\tau(u_\eta^{\mathrm{el}})}\right) = 1 - \exp\left(-\frac{u_\tau}{B_\tau}\right), \tag{41}$$

$$\tilde{\lambda}_\eta^t(u_\eta, \lambda_\eta^c) = u_\eta + \lambda_\eta^c - \frac{\sigma_\eta^t}{k_\eta^t}, \tag{42}$$

$$\tilde{\lambda}_\eta^c(u_\eta, \lambda_\eta^t) = \frac{(\lambda_\eta^t - u_\eta)k_\eta^c - \sigma_\eta^c}{k_\eta^c + 2\sigma_{\eta\eta}^c}. \tag{43}$$

First, we construct the KKT conditions presented in (40)–(43), which emerge by setting the expressions in braces in (32)–(35) to zero. The parameter $\tilde{D}_\eta$ in (40) is separated into two parts such that compression and tension. Tension and compression states are determined by the sign of the elastic part u_η^{el} of normal displacement. The evolution of tangential damage $\tilde{D}_\tau$, as well as the tension $\tilde{\lambda}_\eta^t$ and compression $\tilde{\lambda}_\eta^c$ plastic multipliers, progresses according to (41)–(43), respectively. At the beginning of the deformation process, all presumed irreversible quantities are zero and calculated by correlating the variables from the previous and current time steps. Notably, in cases where plastic deformation does not occur, damage grows depending on the normal displacement. Equation (42) is calculated using the tension σ_η^t plastic yielding parameter, while (43) provides the interpretations involving the compression σ_η^c plastic yielding and hardening $\sigma_{\eta\eta}^c$ parameters. Plastic yielding parameters contribute to the evolution of plastic deformation, whereas the hardening parameter restricts the magnitude of the compression plastic multipliers.

3. Numerical results and discussion

3.1. ***Implementation of the algorithm.*** The critical state phenomenon was presented in our previous work [88]. To address this concept in 2D case, we implemented the algorithm in two stages, as depicted in Figure 1. In Stage 1 (confining stage), biaxial compression is applied up to a specified stress limit value $\bar{\mathbb{S}}$. The stress tensor is defined in (31) using the elastic stiffness tensors and the strain. During

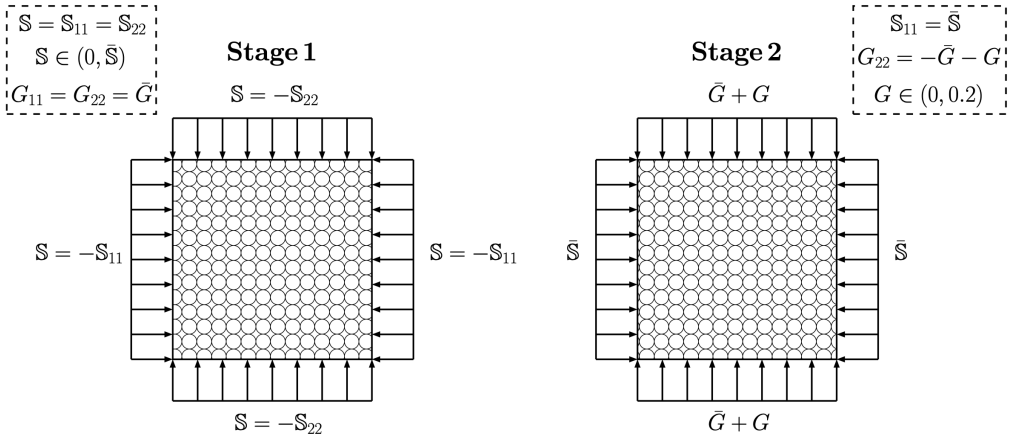

Figure 1. Implementation of Stage 1 and Stage 2 on the homogeneous square model. In Stage 1, $\mathbb{S}$ increases from 0 to $\bar{\mathbb{S}}$, and the strain $\bar{G}$ is reached. In Stage 2 strain, G increases from 0 to 0.2.

Stage 1, the predefined confining stress, $\bar{\mathbb{S}} = -\mathbb{S}_{11} = -\mathbb{S}_{22}$, sequentially increases the strain components (G_{11} and G_{22}) until the specified stress limit is reached. The strain at the end of Stage 1 is denoted by $-\bar{G} = G_{11} = G_{22}$. In Stage 2, the strain in the vertical direction, $G_{22} = -\bar{G} - G$, is incrementally increased by $G > 0$ while the stress in the horizontal direction, $\mathbb{S}_{11}$, remains constant at the confining stress $-\bar{\mathbb{S}}$. During Stage 2, the strain component G_{11} is extruded by fixing the confining stress:

$$G_{11} = -\frac{\bar{\mathbb{S}} + \mathbb{P}_{11} + \mathbb{C}_{1122} G_{22}}{\mathbb{C}_{1111}}. \tag{44}$$

where, in each step, the strain component G_{22} is gradually increased externally, while the shear strain $\bar{G}_{12}$ (or $\bar{G}_{21}$) remains null as considered in (31).

At the beginning of the algorithm's implementation, damage and plastic irreversible phenomena are absent. Notably, the elastic stiffness tensors $\mathbb{C}_{ijab}$ and $\mathbb{P}_{ij}$ are computed at every loading step. The trapezoidal rule is employed for integration calculations over orientation. The elastic stiffness tensors in (13) and (14) are defined with respect to coupled damage and plasticity variables evolving in discretized orientation space. Through KKT conditions, the evolution of damage and plasticity is updated for the next step based on the strain components at each current step. The critical state behavior is defined by both the linearized volumetric strain, $G_V = \det(\boldsymbol{F}) - 1 \simeq G_{11} + G_{22}$, and the principal stress ratio, $\mathbb{S}_{22}/\mathbb{S}_{11}$, as in classical soil mechanics. In line with these behaviors, the cases under which deformation occurs without any change in stress or volume, will be examined in the next Section 3.2.

Algorithm 1 outlines the code for the emergence of the critical state, following the evolution process of damage and plasticity variables. While calculating the strain G_{11}, the value for the current time step is determined using the elastic stiffness parameters $\mathbb{P}_{11}$, $\mathbb{C}_{1111}$, and $\mathbb{C}_{1122}$ obtained from the previous time step. This formulation, as presented in (44), is intended to serve as a numerically explicit scheme, where the strain evolution is directly computed without requiring iterative solutions. Algorithm 1 illustrates this and shows how the next time step values are obtained based on the previous time step. Our approach

For each step:

The strain components G_{11} and G_{22} are calculated with respect to confining stress $\bar{\mathbb{S}}$ in Stage 1.

- $D_\eta(t_0,\theta)=0$, $D_\tau(t_0,\theta)=0$, $\lambda_\eta^t(t_0,\theta)=0$, $\lambda_\eta^c(t_0,\theta)=0\ \forall\theta$ at $t_0=0$.
- $D_\eta(t_{i-1},\theta)=D_\eta$, $D_\tau(t_{i-1},\theta)=D_\tau$, $\lambda_\eta^t(t_{i-1},\theta)=\lambda_\eta^t$, $\lambda_\eta^c(t_{i-1},\theta)=\lambda_\eta^c$ from previous step.

For each orientation θ:

- Compute $\tilde{D}_\eta$, $\tilde{D}_\tau$, $\tilde{\lambda}_\eta^t$, $\tilde{\lambda}_\eta^c$ using threshold functions with D_η, D_τ, λ_η^t, λ_η^c at the current time.
- **If** $\tilde{D}_\eta > D_\eta$, $\tilde{D}_\tau > D_\tau$, $\tilde{\lambda}_\eta^t > \lambda_\eta^t$, $\tilde{\lambda}_\eta^c > \lambda_\eta^c$ **then**
  Set $D_\eta(t_i,\theta)=\tilde{D}_\eta$, $D_\tau(t_i,\theta)=\tilde{D}_\tau$, $\lambda_\eta^t(t_i,\theta)=\tilde{\lambda}_\eta^t$, $\lambda_\eta^c(t_i,\theta)=\tilde{\lambda}_\eta^c$.
  else
  Set $D_\eta(t_i,\theta)=D_\eta$, $D_\tau(t_i,\theta)=D_\tau$, $\lambda_\eta^t(t_i,\theta)=\lambda_\eta^t$, $\lambda_\eta^c(t_i,\theta)=\lambda_\eta^c$.
- Damage and plastic variables are calculated for current step t_i.

- The stiffness tensors $\mathbb{C}_{ijab}$ and $\mathbb{P}_{ij}$ are computed using damage and plastic variables at each step.
- Stage 1 is perfomed up to the stress limit $\bar{\mathbb{S}}=-\mathbb{S}_{11}=-\mathbb{S}_{22}$.
- In Stage 2, the strain component G_{22} is increased while the stress component $\mathbb{S}_{11}=-\bar{\mathbb{S}}$ remains constant.

Algorithm 1. Code outline for the evolution of damage and plasticity phenomena.

simplifies this process by employing an analytical expression for the strain. This reduces computational complexity and provides consistency according to the strain-controlled loading path given in the model.

3.2. *Numerical experiments.*

3.2.1. *Characterization of specimens for emergence of critical state.* To investigate the emergence of critical state, we first characterize the material parameters of three different specimens with varying initial density states (initial void ratios). These specimens are classified as dense, mid-dense, and loose, each presenting distinct dilative/compaction behaviors regarding typical of granular materials. As the inital step in our numerical studies, we use the shear modulus G_{2D}, which was identified by Barchiesi et al. [8] as equivalent to the 2D Lamé coefficient μ_{2D},

$$\mu_{2D}=G_{2D}=\frac{L^2}{8}(k_\eta^c+4k_\tau). \tag{45}$$

Based on experimental data, Chang et al. [13] affirmed the empirical expression of shear modulus G_{emp}, which we incorporated into our model thus:

$$G_{2D}=G_{\text{emp}}=\frac{A}{(e-0.2)^{1.8}}. \tag{46}$$

Here the shear modulus is expressed in terms of the material constant A and the initial void ratio e. The initial void ratio, $e=V_V/V_S$, is defined as the ratio of the void volume V_V to the solid volume V_S. The

$A = 1.4 \times 10^6\,\mathrm{J/m^2}$	$k_\eta^t = 0.1 k_\eta^c\ (\mathrm{J/m^4})$	$k_\tau = 0.1 k_\eta^c\ (\mathrm{J/m^4})$	$B_\eta^t = 0.1 B_\eta^c\ (\mathrm{m})$
$\sigma_\eta^t = 0\,\mathrm{J/m^3}$	$L = 0.01\,\mathrm{m}$	$\alpha = 5 \times 10^{-10}\,\mathrm{m}$	$\alpha_1 = 10$

Table 1. Fixed parameters for all specimens.

material constant A, which is a fixed parameter, is listed in Table 1, while the initial void ratios e for all specimens are given in Table 2. Additionally, the shear modulus, $G_{\mathrm{emp}} = G_{2D}$, is calculated based on (46), utilizing the material constant A and initial void ratio e. Further, k_η^c is determined based on (45) and (46) utilizing the assumed relationship between k_η^c and k_τ as specified in Table 1 for all materials using the following expression (see Table 2):

$$k_\eta^c = \frac{8G_{2D}}{L^2} - 4k_\tau. \tag{47}$$

The material parameters that are kept constant for all specimens are the material constant A, the stiffness parameters k_η^t and k_τ, the normal characteristic damage displacement B_η^t in tension, the plastic yielding parameter σ_η^t in tension, the intergranular interaction distance L, and the constitutive parameters α and α_1. These parameters are presented in Table 1. By contrast, $\bar{e}$, $\bar{G}_{2D}$, $\bar{k}_\eta^c$, $\bar{B}_\eta^c$, $\bar{\sigma}_\eta^c$, and $\bar{\sigma}_{\eta\eta}^c$ are the simulation parameters used in [88] for each specimen and are associated with the emergence of the critical state.

The initial void ratio e, the shear modulus G_{2D}, the compression normal stiffness k_η^c, the damage characteristic displacements B_η^c and $B_{\tau 0}$, and the plasticity constitutive parameters σ_η^c and $\sigma_{\eta\eta}^c$ are listed for all considered specimens in Table 2.

Figure 2 provides a comparative visualization of square specimens referred to as dense, mid-dense, and loose and shows the particle arrangement associated initial void ratio. Each specimen is depicted to highlight the sectional distribution of solid particles and voids. In a dense specimen (Figure 2, left), the particle arrangement has a high solid density and minimal void space with a low initial void ratio. A mid-dense specimen (Figure 2, middle) has a composition less packed than a dense one, with a medium

specimen	e	$G_{2D}\ (\mathrm{J/m^2})$ [see (46)]	$k_\eta^c\ (\mathrm{J/m^4})$ [see (47)]
dense	$\bar{e}_D = 0.5$	$\bar{G}_{2D_D} = 1.22 \times 10^7$	$\bar{k}_{\eta_D}^c = 7.0 \times 10^{11}$
mid-dense	$\bar{e}_M = 0.7$	$\bar{G}_{2D_M} = 4.55 \times 10^6$	$\bar{k}_{\eta_M}^c = 2.6 \times 10^{11}$
loose	$\bar{e}_L = 1.2$	$\bar{G}_{2D_L} = 1.45 \times 10^6$	$\bar{k}_{\eta_L}^c = 8.3 \times 10^{10}$

$B_\eta^c\ (\mathrm{m})$	$B_{\tau 0}\ (\mathrm{m})$	$\sigma_\eta^c\ (\mathrm{J/m^3})$	$\sigma_{\eta\eta}^c\ (\mathrm{J/m^4})$
$\bar{B}_{\eta_D}^c = 0.0050\,L$	$0.24 B_\eta^c$	$\bar{\sigma}_{\eta_D}^c = 0.06 k_\eta^c L$	$\bar{\sigma}_{\eta\eta_D}^c = 0.28 k_\eta^c$
$\bar{B}_{\eta_M}^c = 0.0105\,L$	$0.20 B_\eta^c$	$\bar{\sigma}_{\eta_M}^c = 0.23 k_\eta^c L$	0
$\bar{B}_{\eta_L}^c = 0.0310\,L$	$0.20 B_\eta^c$	$\bar{\sigma}_{\eta_L}^c = 0.72 k_\eta^c L$	0

Table 2. Simulation parameters for dense, mid-dense, and loose specimens.

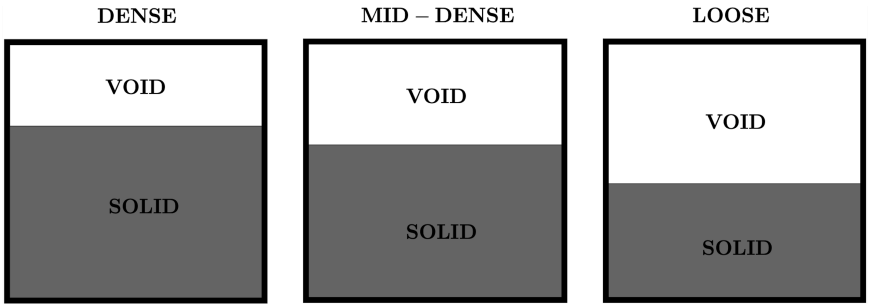

Figure 2. Schematic representation of dense ($e = 0.5$), mid-dense ($e = 0.7$), and loose ($e = 1.2$) specimens comparing the solid particles arrangement and voids in relation to the initial void ratio.

initial void ratio regarding the solid particles. A loose specimen (Figure 2, right) has significantly larger void spaces and a higher initial void ratio.

3.2.2. *Emergence of the critical state.* We first introduce the principal stress ratio $\mathbb{S}_{22}/\mathbb{S}_{11}$ and volumetric strain G_V depending on vertical strain G to elucidate the predicted macroscale critical state behavior for all specimens with different initial density states in Figure 3. In Stage 1, the confining stress $-\mathbb{S}_{11} = -\mathbb{S}_{22} = \bar{\mathbb{S}}$ is set to 100 kN/m. The strain G describes the subjected strain in the vertical direction as depicted in Figure 1. The typical critical state behavior is defined as no change in both stress and volumetric strain under high shear deformation $G > 0.12$. Figure 3 suggests that our numerical simulations accurately predict this classical critical state behavior. It is noteworthy that deformation continues even after this classical response is achieved. Additionally, regarding the importance of deformation evolution, we examine the relationship between stress ratio and volumetric strain behaviors. This relationship is characterized by increase/decrease in stress $\mathbb{S}_{22}$, which indicates dilative ($G_V > 0$) or contractive ($G_V < 0$) behaviors in volumetric strain. For a dense specimen, a significant peak followed by a post-peak behavior is observed in the principal stress ratio, along with dilative behavior in volumetric strain. As we move towards a loose specimen, the peak in the stress ratio disappears, and a contractive behavior in volumetric

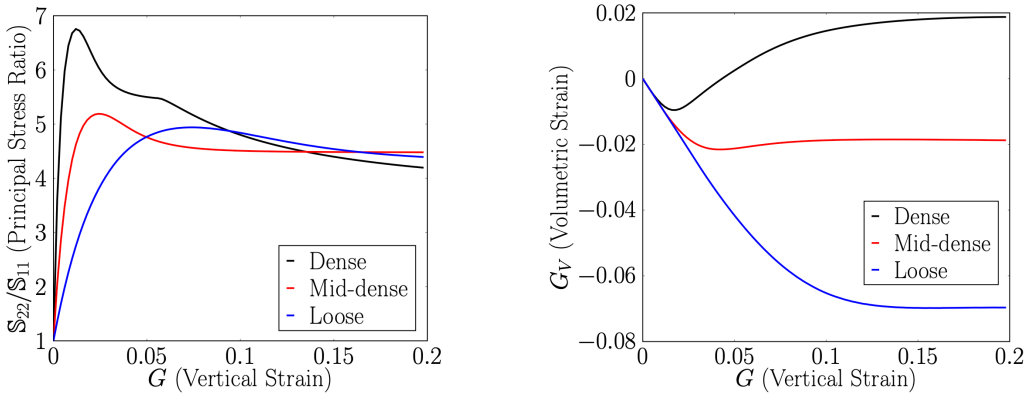

Figure 3. Critical state behavior under $\bar{\mathbb{S}}$=100 kN/m with principal stress ratio $\mathbb{S}_{22}/\mathbb{S}_{11}$ (left) and volumetric strain G_V (right).

strain is observed. After hardening and softening behaviors are observed for all considered specimens, dilative behavior is noted for a dense specimen, and contractive behavior is stimulated for the mid-dense and loose specimens. Indeed, in light of these results and comparison with the experimental findings presented by Lee and Seed [45], a numerical model qualitatively predicts both dilative behavior (for a dense specimen) and contractive behavior (for the mid-dense and loose specimens) with respect to different initial density states.

According to the KKT conditions presented in (40)–(43), the damage and plastic irreversible quantities, which are illustrated in Figures 4–7, arose considering only homogeneous deformation from the grain-pair interactions. The evolution of these irreversible phenomena is orientation-based, therefore the circles represent the amount of damage and plasticity in each orientation. All polar plots have a certain number of circles because each specified interval of the strain is partitioned into 10 equal steps.

Figures 4 and 5 show the evolutions of normal damage (D_η) and tangential damage (D_τ) as a result of grain-pair interactions for all specimens along with specific strain ranges. These polar plots identify Stage 1 in column i) and Stage 2 in columns ii), iii), iv), and v) with respect to the selected four different vertical strain (G) intervals. We first present the normal damage polar plots in Figure 4, deploying (40). In Stage 1, the normal damage progresses equally in all orientations for all specimens because the confining stress is implemented equally in both directions as equi-biaxial loading. However, the normal damage in a loose

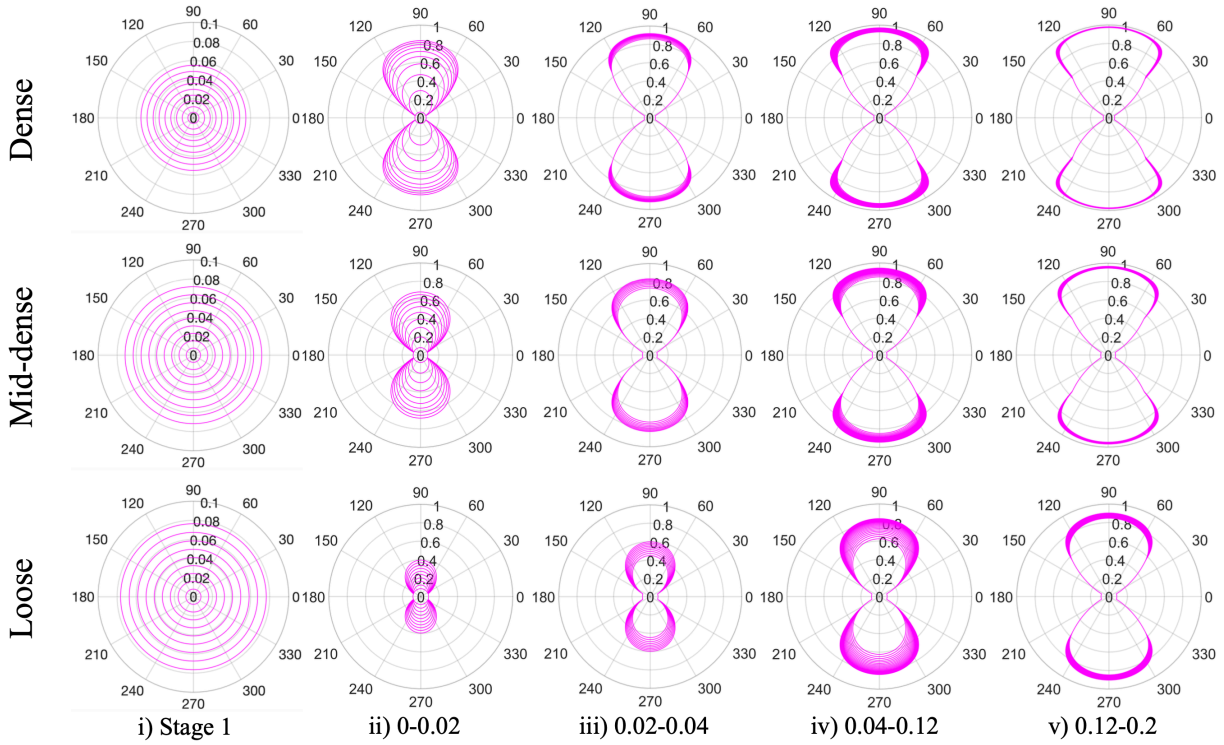

Figure 4. Normal damage D_η polar plots for dense, mid-dense, and loose specimens at Stages 1 and 2 from i) to v) for different strain intervals.

specimen progresses faster than in a dense specimen due to rearrangement and settlement during the confinement process, which causes the specimens to become stiffer. Notably, during Stage 1, tangential damage does not grow because the tangential displacement vector is null; see (6).

Normal and tangential damage increases rapidly in all specimens within the strain range $G \in (0, 0.04)$ and approaches unity value at the beginning of Stage 2 as illustrated in columns ii) and iii) of Figure 4. For the strain range $G > 0.12$ at the critical state history, the damage variables stabilize and approach a maximum evolution value, as seen in columns iv) and v) of Figure 4. In Stage 2, a dense specimen reaches peak strength at lower strain values, and a faster loss of stiffness occurs in a dense specimen compared to a loose specimen, as shown in Figure 3. Normal damage increases in the compressed vertical direction, corresponding to the loading path in the orientation ranges of 45°–135° and 225°–315°, while the growth remains constant at the value reached at the end of Stage 1 in the horizontal direction. At this moment, an in-depth investigation of this phenomenon is required to understand the dependence of constitutive parameters during the evolution process. When the horizontal directions of the specimens are in tension, because of positive Poisson's effect ($G_{11} \gg G_{22}$), it is expected that the tensile B_η^t characteristic damage displacement is smaller than that in compression B_η^c as written in Table 1, provoking faster damage evolution. However, in the horizontal direction, plasticity is activated with a null tensile σ_η^t plastic yielding parameter, and the tensile displacement becomes plastic because the normal displacement u_η^{el} is positive. The normal damage threshold $\tilde{D}_\eta$ values in (40) do not increase under this loading path without first reaching the previous step's threshold values in the horizontal direction.

Tangential damage evolves over a wider range of orientations compared to the predicted normal damage. Let us analyze the evolution in a dense specimen, the predicted tangential damage approaches a near unity value at 45° orientations faster than in the loose and mid-dense specimens in column ii) of Figure 5. The evolution of tension plastic multipliers λ_η^t alters the elastic normal displacement u_η^{el} in the horizontal direction and influences the characteristic tangential damage displacement B_τ. When transitioning from compression to tension, an increase in the threshold value via (41) is expected for tangential damage at the horizontal direction limits, due to the decrease in B_τ at the rate of regularization parameter α_1 based on (19). The strain component G_{11} increases; therefore the normal u_η displacement becomes positive. The trend for a dense specimen is also observed in a mid-dense specimen, but at a slower rate. For both dense and mid-dense specimens, in the strain band $0 < G < 0.04$, tangential damage reaches its maximum value and saturates across most orientations. At the beginning of Stage 2, a loose specimen is in compression for all orientations, due to negative Poisson's effect ($G_{22} \gg G_{11}$), and tangential damage begins to grow slowly, adopting a flower shape as seen in column ii) of Figure 5. The reason is that a loose specimen has a higher B_τ value than other specimens. When the vertical strain is in the range $0.02 < G < 0.04$, tangential damage first evolves rapidly in the horizontal direction. As the tension plastic multipliers λ_η^t grow within this strain range, orientations in the horizontal direction come under tension, resulting rapid evolution. In column v) of Figure 5, tangential damage reaches a unity value in the quarter directions for all specimens.

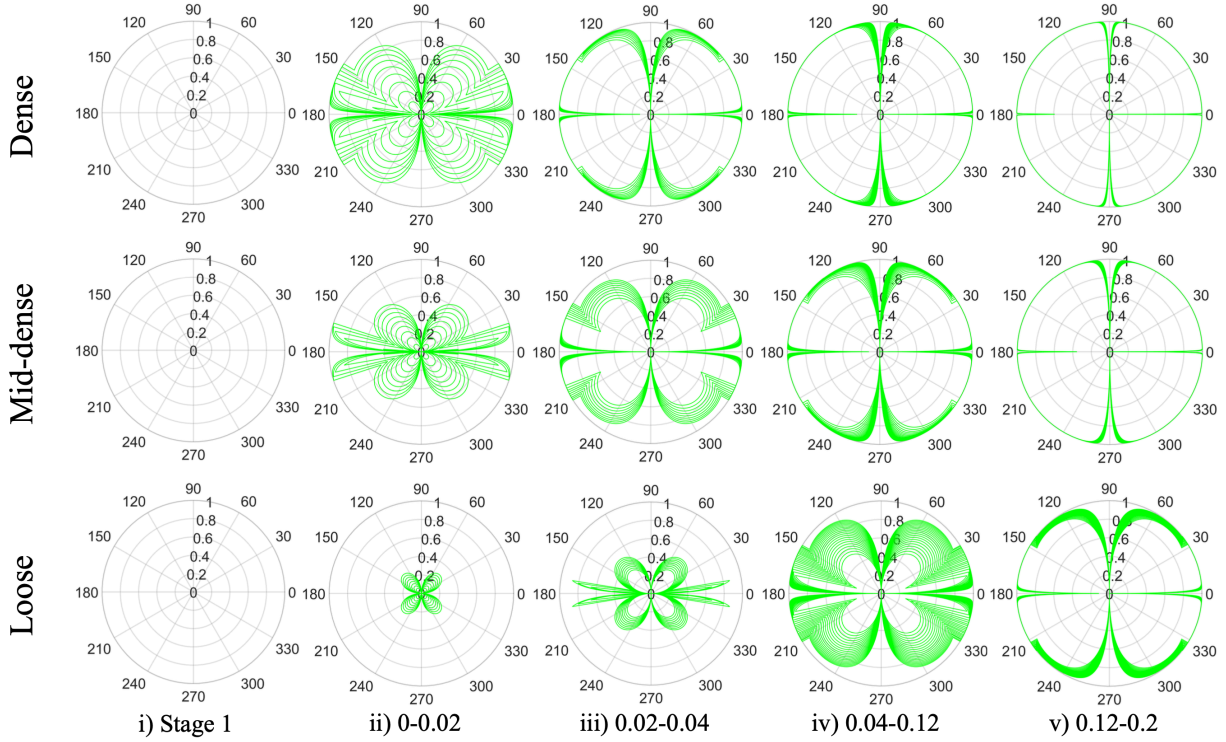

Figure 5. Tangential damage D_τ polar plots for dense, mid-dense, and loose specimens at Stages 1 and 2 from i) to v) for different strain intervals.

While we deduce that the evolution of damage is defined as loss of stiffness in line with (13) and (14) in a GMA, it can also be considered as material loss in the directions it grows within the granular structure. By following a series of grain-pair interaction mechanisms, rotation and sliding movements are effective in the collapse of particle chains and cause loss of stiffness. These normal and tangential damage variables occur as the main results of these movements. Tangential damage refers to the loss of lateral support among grain neighbors, whereas normal damage is defined as the illustration of collapse of the grains.

The evolutions of tension λ_η^t and compression λ_η^c plastic multipliers are shown in Figures 6 and 7. Plastic deformations evolve orientationally due to the sliding movement of grains, representing irrecoverable plastic displacements. During Stage 1, plastic multipliers are not observed because the threshold value does not progress enough to exceed the initial value according to (42) and (43). The evolution of plastic multipliers is presented in the determined five strain range during Stage 2.

The tension λ_η^t plastic multipliers predominantly grow in the horizontal direction for all specimens (see Figure 6). As a consequence of the applied compression in the vertical direction and the fixed stress in the horizontal direction, the strain component G_{11} increases and triggers an effective horizontal tension behavior with regard to Poisson's effect. This causes the normal u_η displacement to become positive. In order to elapse from hardening behavior to softening behavior earlier in strain in Stage 2, the tension

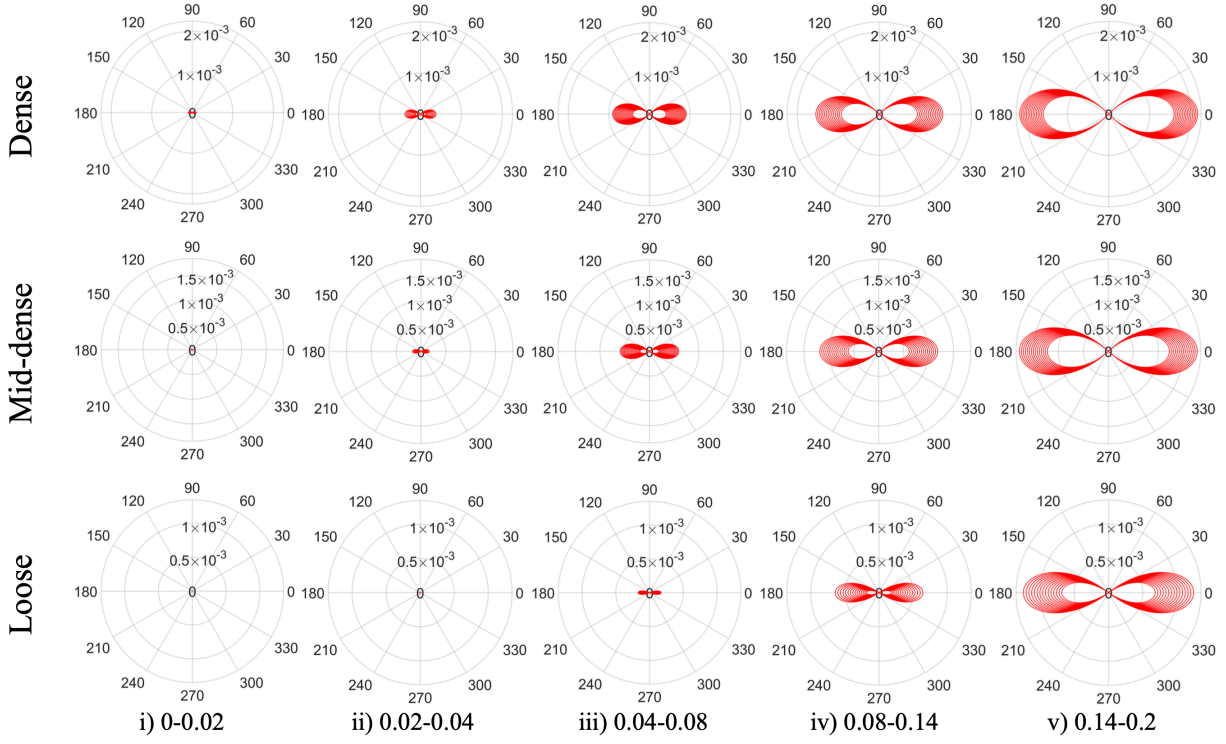

Figure 6. Tension λ_η^t plastic multiplier polar plots for dense, mid-dense, and loose specimens at vertical strain from i) to v) for different strain intervals.

σ_η^t plastic yielding parameter is characterized as null for all specimens, and the threshold function in (42) is triggered to increase. In a dense specimen, early initiation of the tension λ_η^t plastic multipliers compared to the mid-dense and loose specimens is required to reach dilative behavior. The tension plastic multipliers are higher in a dense specimen than in other specimens within a certain range of the horizontal direction.

The evolution of compression λ_η^c plastic multipliers for a dense specimen is shown in Figure 7. We further investigate how the evolution of compression plastic multipliers triggers contractive behavior. To

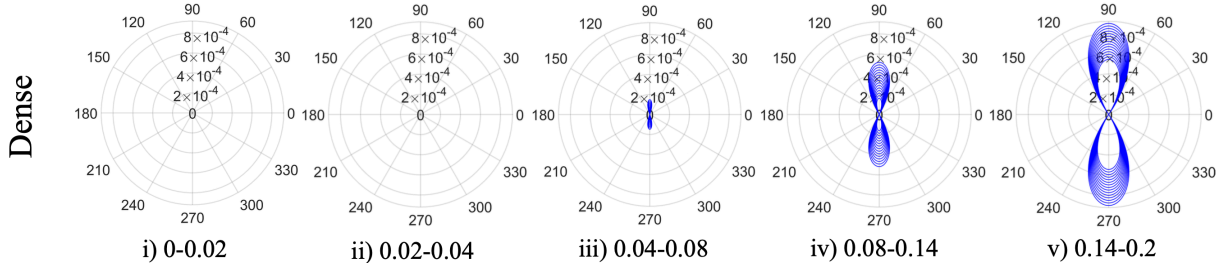

Figure 7. Compression λ_η^c plastic multiplier polar plots for dense specimen at vertical strain from i) to v) for different strain intervals.

achieve the critical state in the mid-dense and loose specimens, a higher plastic compression σ_η^c yielding parameter is adapted, and the compression plastic multipliers are not activated during simulations. In fact, the critical state is reached after the contractive behavior ends in the mid-dense and loose specimens (see Figure 3, right). Additionally, these plastic multipliers predominantly grow only for a dense specimen in the vertical direction. The hardening parameter ($\sigma_{\eta\eta}^c$) plays an important role in reaching the critical state during the dilative behavior in the volumetric strain. By adjusting the hardening parameter and limiting the increase in volumetric strain, the typical critical state response is observed for a dense specimen as seen in Figure 3, right. Additionally, the parametric studies on the plastic compression yielding and hardening parameters are conducted by investigating the principal stress ratio and volumetric strain as discussed in the next Section 3.2.3.

3.2.3. *Parametric studies on a granular micromechanics continuum model.* In the present numerical framework, the constitutive relations are established based on multiple parameters. The simulation parameters, which are defined in distinctive assumptions, are found using nondimensionalization coefficients (as shown in Tables 1 and 2), ensuring consistent units of measure across the compression constitutive parameters. These assumptions are made to reach the idealized behavior of critical state with regard to the deformation evolution. To expose the behavior of numerical model, a set of parametric studies are conducted by varying only one parameter for the dense, mid-dense, and loose specimens for each simulation, in terms of the principal stress ratio ($\mathbb{S}_{22}/\mathbb{S}_{11}$) and volumetric strain ($G_V = G_{11} + G_{22}$). The model predictions in loading Stage 2 (shearing stage) are presented with respect to the imposed strain component $G = -G_{22} - \bar{G}$. The rest of parameters are kept constant throughout all parametric studies. For our investigation into the predictive accuracy of numerical model, the insights gained from these studies can lead to more reliable predictions in the future works. The numerical analyses focus on compression k_η^c normal stiffness, characteristic compression B_η^c normal displacement, compression σ_η^c plastic yielding and hardening $\sigma_{\eta\eta}^c$ parameters. Notably, in Stage 1 (confining stage), the confining stress $\bar{\mathbb{S}}$ is set to 100 kN/m for all simulations. Along the parametric studies, $\bar{k}_\eta^c$, $\bar{B}_\eta^c$, $\bar{\sigma}_\eta^c$, and $\bar{\sigma}_{\eta\eta}^c$ represent the constitutive parameters values employed in [88] for the critical state, with only the nondimensionalization coefficients being varied (see Tables 1 and 2).

We first used the compression k_η^c normal stiffness parameter in the numerical simulations. In Figure 8, the predicted principal stress ratio and volumetric strain behaviors are presented for three different specimens. In each simulation, only the values of $\bar{k}_{\eta_D}^c$, $\bar{k}_{\eta_M}^c$, and $\bar{k}_{\eta_L}^c$ for the dense, mid-dense, and loose specimens, respectively, were increased or decreased by multiplying with a nondimensionalization coefficient. It is noteworthy to remark that all parameters related to the compression k_η^c normal stiffness parameter in Tables 1 and 2 were updated automatically. An increase in the compression normal stiffness triggers an increase in the shear modulus (G_{2D}) at the same rate, as seen in (45), which leads to a decrease in the initial void ratio (e), according to the relationship between shear modulus and initial void ratio in (46). Thus, the stiffening behavior of the material can be observed by correlating the changes in compression normal stiffness with the initial void ratio. Notably, as given in (46), the initial void ratios do

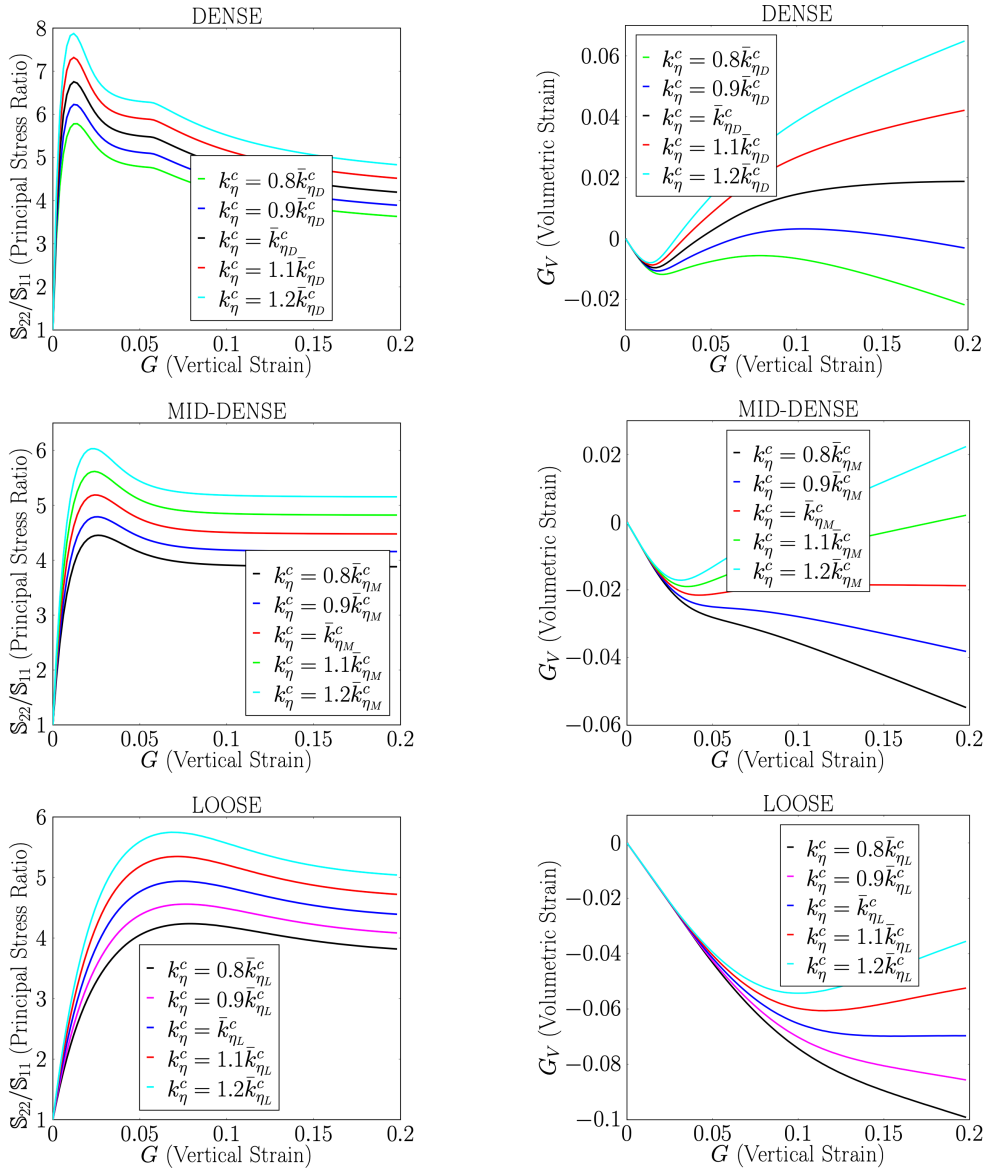

Figure 8. Parametric analysis by changing compression $\bar{k}_\eta^c$ normal stiffness for all specimens in terms of the principal stress ratio $\mathbb{S}_{22}/\mathbb{S}_{11}$ (left column) and volumetric strain G_V (right column).

not change at the same rate as the nondimensionalization coefficients of the compression normal stiffness parameter. The initial void ratio ranges from $e \in (0.47, 0.54)$ for dense, $e \in (0.67, 0.79)$ for mid-dense, and $e \in (1.09, 1.31)$ for loose specimens, depending on the highest and lowest compression normal stiffness values. For a dense specimen, the principal stress ratio for all varied compression $\bar{k}_{\eta_D}^c$ normal stiffness parameters (Figure 8, top left) exhibits a significant peak, subsequently followed by remarkable post-peak softening that asymptotically approaches a residual principal stress ratio over the same vertical

strain, and a small contraction is predicted around a characteristic zero volume change point, followed by de-densification and eventual volume dilation at different vertical strains, particularly at high compression normal stiffness parameters (Figure 8, top right). For a mid-dense specimen, the principal stress ratio in Figure 8, middle left, serves moderate softening with a distinct peak for all cases of compression $\bar{k}^c_{\eta_M}$ normal stiffness, followed by no change in principal stress ratio. Regarding the volumetric strain, Figure 8, middle right, shows a contractive response at low compression normal stiffness. Similarly, for a loose specimen, the principal stress ratio in Figure 8, bottom left, illustrates gradual softening with a defined peak only at high compression $\bar{k}^c_{\eta_L}$ normal stiffness, followed by an asymptotic decrease in the residual principal stress ratio, while the volumetric strain presents a contractive behavior across all compression normal stiffness parameters in Figure 8, bottom right. A proportional increase in the stiffness value is predicted when the compression normal stiffness is increased, since the elastic stiffness tensors are derived via (13) and (14).

Secondly, the characteristic compression B^c_η normal displacement is adopted for the parametric studies, and the principal stress ratio and volumetric strain responses are shown depending on the parameters $\bar{B}^c_{\eta_D}$, $\bar{B}^c_{\eta_M}$, and $\bar{B}^c_{\eta_L}$ with respect to the dense, mid-dense, and loose specimens, respectively, in Figure 9. In the threshold functions (40) and (41), the evolution equations of normal and tangential damage were also derived based on characteristic damage displacements. The characteristic tension normal displacements B^t_η and tangent $B_{\tau 0}$ are provided in terms of the characteristic compression normal displacement in Tables 1 and 2. As observed in Figures 4 and 5, the damage evolution in a dense specimen progresses faster than in a loose specimen with respect to low the characteristic compression normal displacement (see Table 2 for the value of the B^c_η parameter of all specimens). During all simulations, only the $\bar{B}^c_\eta$ values of the specimens were multiplied with nondimensionalization coefficients. For a dense specimen, a significant peak is observed in the principal stress ratio (Figure 9, top left) at different strain values, followed by remarkable post-peak softening and an asymptotic decrease. After the softening behavior occurs up to the same certain strain in volumetric strain, volume dilation occurs at high the characteristic compression $\bar{B}^c_{\eta_D}$ normal displacement parameters (Figure 9, top right). After a peak is observed in the principal stress ratio, softening and no change in the stress are observed in a mid-dense specimen (Figure 9, middle left), while volumetric strain (Figure 9, middle right) exhibits dilative behavior at high the characteristic compression $\bar{B}^c_{\eta_M}$ normal displacement. In a loose specimen, the peak in the principal stress ratio disappears at low the characteristic $\bar{B}^c_{\eta_L}$ compression normal displacement (Figure 9, bottom left), and a contractive response raises at all the characteristic compression normal displacement parameters (Figure 9, bottom right). The characteristic compression normal displacement plays a vital role in determining the elastic stiffness tensors in (13) and (14) and material strength properties because it regulates damage evolution.

According to the first two parametric studies based on the compression k^c_η normal stiffness and characteristic compression B^c_η normal displacement, there are both similarities and differences in the volumetric strain and principal stress ratio behaviors. Softening behavior after the significant peak was commonly observed for the principal stress ratio at high values. Volumetric strain exhibited dilative behavior at high and contractive behavior at low values of these constitutive parameters. When the

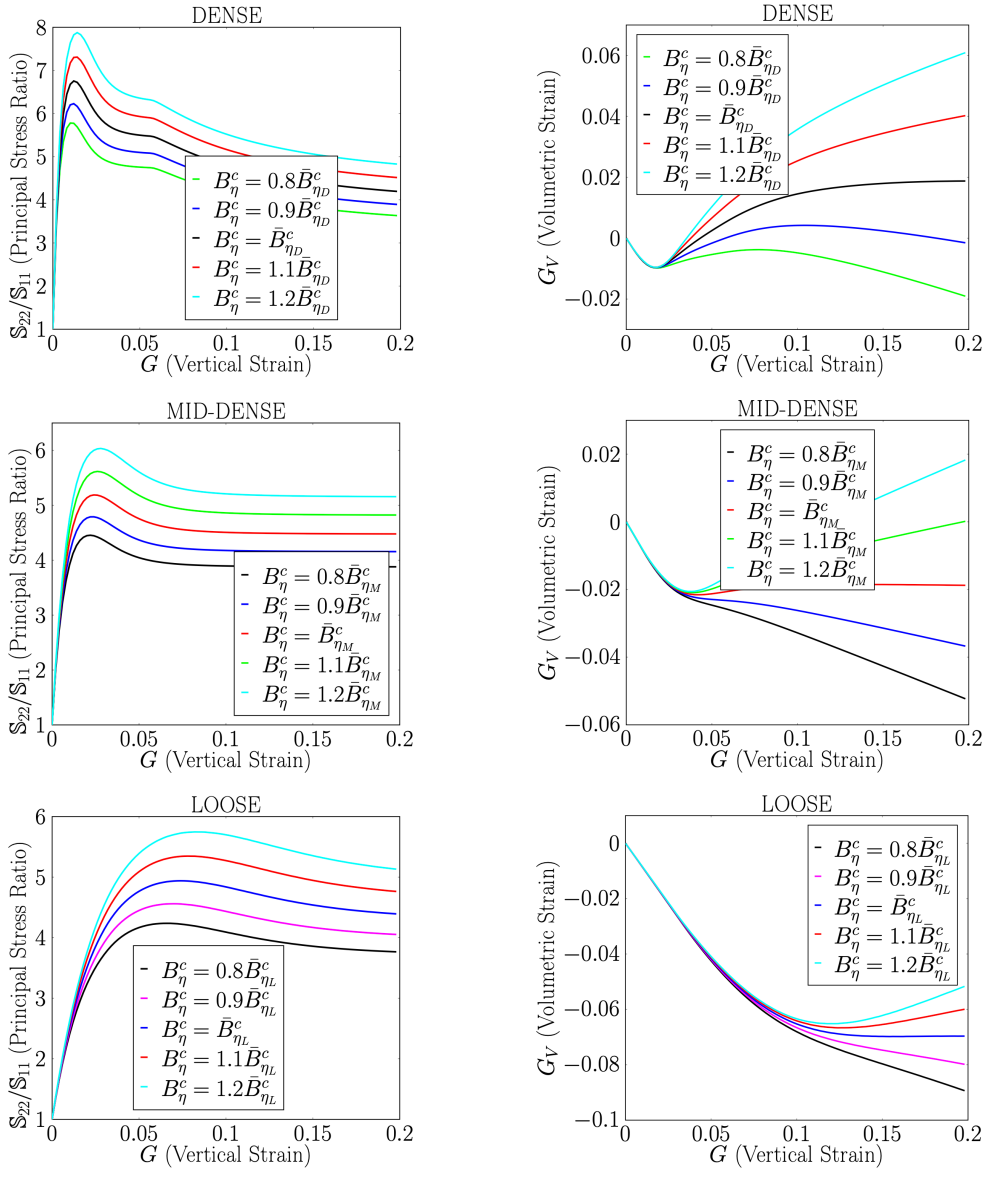

Figure 9. Parametric analysis by changing compression $\bar{B}^c_\eta$ characteristic normal displacement for all specimens in terms of the principal stress ratio $\mathbb{S}_{22}/\mathbb{S}_{11}$ (left column) and volumetric strain G_V (right column).

compression normal stiffness is varied, the peak in the principal stress ratio occurs at the same strain in all specimens (Figure 8, left column), while the volumetric strain differs across different strains (right column). Conversely, for characteristic compression normal displacement, the principal stress ratio peaks at different strain values for each specimen in the left column of Figure 9, but the volumetric strain starts from the same strain value and then shows either dilative or contractive behavior as documented in the right column of the same figure.

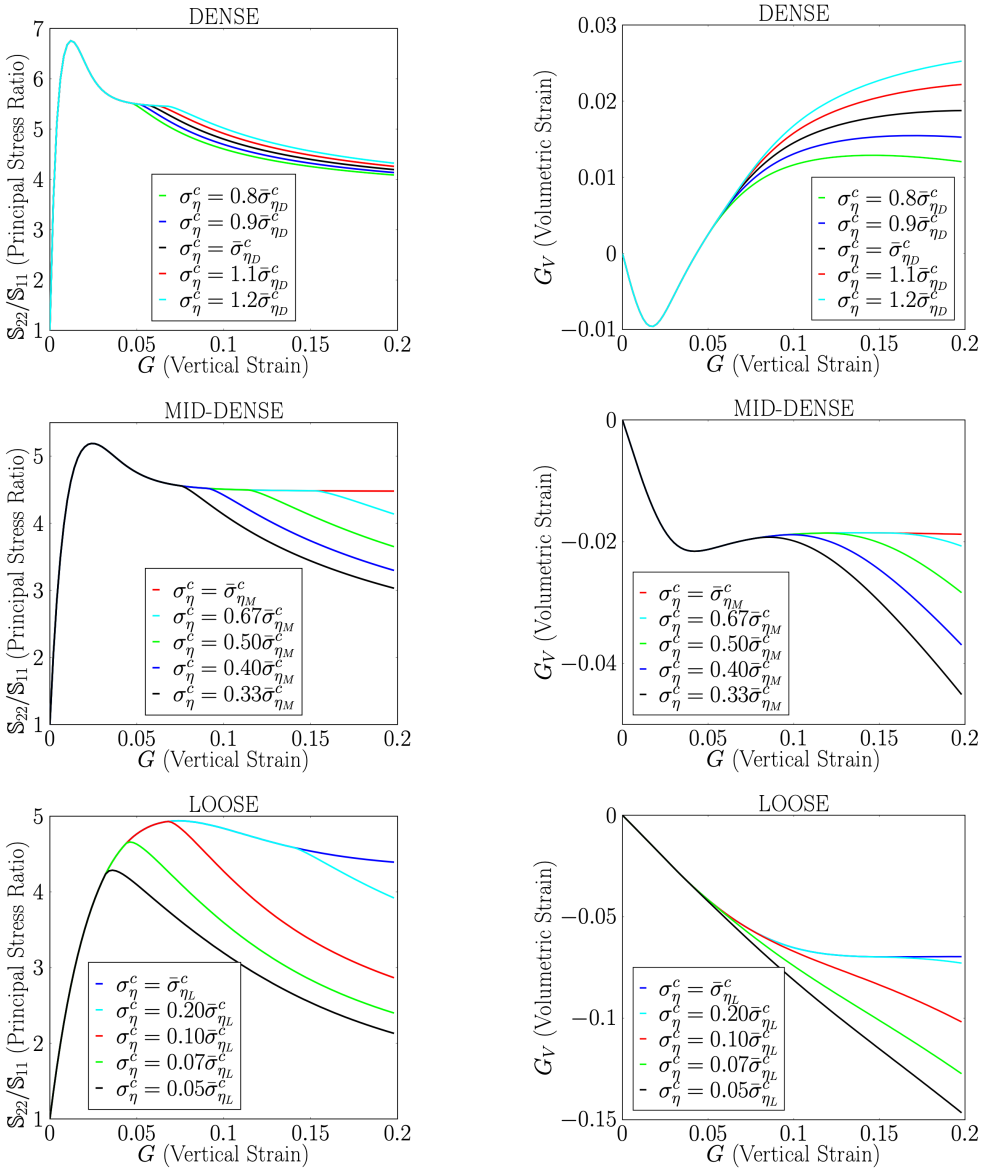

Figure 10. Parametric analysis by compression $\bar{\sigma}_\eta^c$ plastic yielding parameter for all specimens in terms of the principal stress ratio $\mathbb{S}_{22}/\mathbb{S}_{11}$ (left column) and volumetric strain G_V (right column).

Thirdly, the compression σ_η^c plastic yielding parameter is obtained by the multiplying of compression k_η^c normal stiffness and the intergranular distance L in terms of catching the same unit of measure. The principal stress ratio and volumetric strain were examined in relation to $\bar{\sigma}_{\eta_D}^c$, $\bar{\sigma}_{\eta_M}^c$, and $\bar{\sigma}_{\eta_L}^c$ values of dense, mid-dense, and loose specimens, respectively, for all specimens as shown in Figure 10. The compression plastic yielding parameter plays a crucial role in determining the strain at which the evolution of compression λ_η^c plastic multipliers can start and how much their quantities increase. During the

numerical simulations, only the nondimensionalization coefficient belonging to compression plastic yielding parameter was varied. In fact, this was done to examine how affected the behavior of numerical model by either accelerating or delaying the evolution of compression plastic multipliers. For a dense specimen, the significant peak of principal stress ratio occurs at the same strain for all multiplied compression $\bar{\sigma}^c_{\eta_D}$ plastic yielding parameter parameters, while the post-peak occurs at different strains depending on the evolution of compression plastic multipliers, resulting in an asymptotic decline, as seen in Figure 10, top left. After the softening and subsequent hardening behaviors arise at volumetric strain up to a certain strain, dilative behavior is observed for high compression plastic yielding parameter in Figure 10, top right. In more detail, with the postponed evolution of λ^c_η, the strain component G_{11} becomes more dominant than the other strain component G_{22}, and there is an increase in volumetric strain. Upon reaching the classical critical state response, the evolution of compression plastic multipliers was not observed in the mid-dense and loose specimens. Therefore, in these specimens, the compression $\bar{\sigma}^c_{\eta_M}$ and $\bar{\sigma}^c_{\eta_L}$ plastic yielding parameters were reduced, and the compression plastic multipliers evolved, allowing the remaining analyses to be completed. In both specimens, the principal stress ratio decreased asymptotically at lower strains, (Figure 10, middle left and bottom left), while contractive behavior occurred with the strain component G_{22} becoming more dominant in volumetric strain (Figure 10, middle and bottom right). From these simulations, it appears that the evolution of compression plastic multipliers affects the second-order tensor $\mathbb{P}_{ij}$ given in (14), causing changes in both the stress component $\mathbb{S}_{22}$ and the strain component G_{11} in (44).

Finally, the parametric analysis was accomplished varying the hardening parameter $\sigma^c_{\eta\eta}$, which is associated with the compression k^c_η normal stiffness (having the same unit of measure) and a nondimensionalization coefficient. Only the principal stress ratio and volumetric strain for a dense specimen are presented based the hardening parameter $\bar{\sigma}^c_{\eta\eta_D}$ in Figure 11. Depending on whether the hardening parameter is increased or decreased, the quantities of compression plastic multipliers are adjusted, following (43). For a dense specimen, a significant peak in the principal stress ratio was observed at the

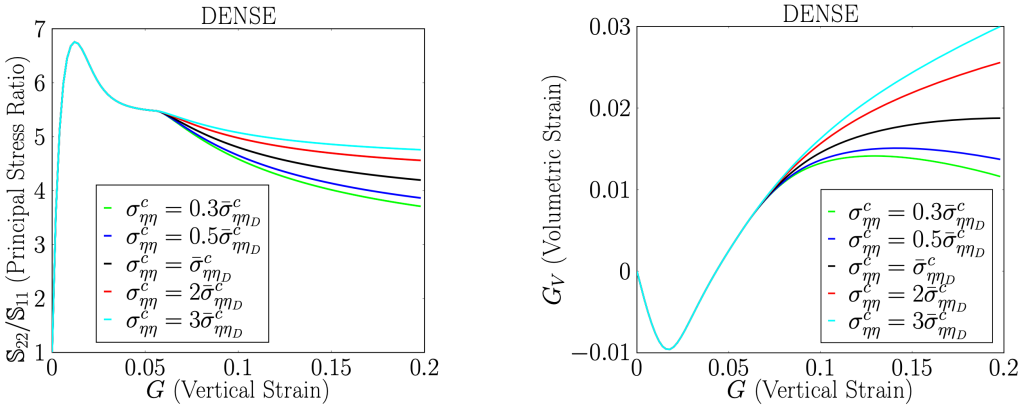

Figure 11. Parametric analysis by hardening $\bar{\sigma}^c_{\eta\eta}$ parameter for dense specimen in terms of the principal stress ratio $\mathbb{S}_{22}/\mathbb{S}_{11}$ (left) and volumetric strain G_V (right).

same strain, followed by a change at the same strain where the subsequent post-peak occurred for all hardening parameter values (Figure 11, left). At high values of the hardening parameter, the evolution of compression plastic multipliers decelerates, and both the principal stress ratio and volumetric strain increase, resulting in dilative behavior (Figure 11, right). Conversely, at low hardening parameter, the evolution of compression plastic multipliers accelerates, causing the principal stress ratio to decrease asymptotically. While the volumetric strain still exhibits dilative behavior, the amount tends to decrease compared to the preceding work's outcomes. These studies indicate that the evolution of compression plastic multipliers affects the second-order tensor $\mathbb{P}_{ij}$ in (14), impacting both the stress component $\mathbb{S}_{22}$ in (29) and the strain component G_{11} in (44).

4. Conclusion

This paper is devoted for a parametric study to investigate the behavior of a previously constructed and validated numerical framework that examines the macroscale critical state. To extend a previous work [88], we focus on revealing stress and volumetric strain responses during simulations by varying characteristic compression constitutive parameters with nondimensionalization coefficients. In addition, the predicted irreversible kinematic quantities are used for the emergence of critical state within a granular micromechanics approach (GMA). The elastic and dissipation energies are designated based on the grain-pair interaction mechanisms by describing the damage-elastoplastic springs deployed into both normal and tangential directions to link micro-macro mechanisms. A hemivariational approach is employed to derive Karush–Kuhn–Tucker (KKT) conditions, thereby the evolution equations for coupled damage and plasticity phenomena are obtained from appropriately formulated energy equations. These kinematic irreversible quantities do not decrease over time and evolve with regard to orientation-based growth depending on the loading path. In a GMA, damage variables define the loss of stiffness representing collapse or buckling of grain chains. Plasticity phenomena refers to irreversible deformation such that rotation or grain sliding. Our approach is independent from classical macroplasticity by focusing on micro-level plasticity. At the microscale, plasticity is governed by the KKT conditions (see (43)). These conditions serve a plasticity criterion. However, these conditions do not directly apply at the macro-level, where classical macroplasticity lacks an explicit criterion for the emergence of plastic behavior. Formal identification between a plasticity criterion and a flow-rule used in macroplasticity is not directly incorporated or emergent in our proposed micro-level model. The current approach does not aim to derive macroscale models such as a flow-rule or macro-level plasticity. Indeed, our model focuses on capturing the grain-scale mechanisms and their direct contributions to the material's overall response, offering a different perspective from traditional macroplasticity formulations.

The continuum model integrates a large number of grain contacts from a mechanical point of view and presents the average behavior over the grain-pair orientations space. The strain where the stress peak occurs, and the lowest volume strain occurs may differ depending on which material parameter is changed. In this sense, the model tends towards dilative (or contractive) behavior at (or around) the

certain strains where the stress ratio increases (or decreases). Poisson's effect shows a nonlinear response according to the evolution of directional damage growth (loss of stiffness) and irrecoverable deformation (plastic), which triggers anisotropic behavior in the volumetric strain.

Overall, as shown in Figures 8–11, when different material parameters are adapted into the simulations, changes in the principal stress ratio and volumetric strain behavior of the specimens appear. In order to achieve the critical state, both principal stress ratio and volumetric strain remain constant while the deformation continues to progress, even under significant shearing. It should be emphasized that the critical state may not be observed depending on changes in material parameters, since one behavior may tune to the typical response while the other might not conform to this classical concept. In fact, improperly defined material parameters in the model might cause behaviors that deviate from the desired response by significantly influencing the stress-strain relationship and deformation characteristics. the material can become correspondingly stiffer/looser due to the increase/decrease in the compression constitutive parameters, leading to more/less deformation evolution. It is remarkable that while the macroscale behavior is predicted according to different loading paths, the irreversible grain-scale deformation processes play an important role. This study provides the guidance for improving the predictions that a numerical model will provide for the future studies under various loading scenarios by refining the energy functions and properly assigning the constitutive parameters.

References

[1] B. E. Abali, W. H. Müller, and V. A. Eremeyev, "Strain gradient elasticity with geometric nonlinearities and its computational evaluation", *Mech. Adv. Mater. Modern Proc.* **1** (2015), art. id. 4.

[2] B. E. Abali, W. H. Müller, and F. dell'Isola, "Theory and computation of higher gradient elasticity theories based on action principles", *Arch. Appl. Mech.* **87**:9 (2017), 1495–1510.

[3] D. Addessi, F. D'Annibale, L. Placidi, and I. Giorgio, "A bone remodeling approach encoding the effect of damage and a diffusive bio-mechanical stimulus", *Contin. Mech. Thermodyn.* **36**:4 (2024), 993–1012.

[4] J. Altenbach, H. Altenbach, and V. A. Eremeyev, "On generalized Cosserat-type theories of plates and shells: a short review and bibliography", *Arch. Appl. Mech.* **80**:special issue (2010), 73–92.

[5] N. Auffray, F. dell'Isola, V. A. Eremeyev, A. Madeo, and G. Rosi, "Analytical continuum mechanics à la Hamilton–Piola least action principle for second gradient continua and capillary fluids", *Math. Mech. Solids* **20**:4 (2015), 375–417.

[6] G. Aydin, M. E. Yildizdag, and B. E. Abali, "Strain-gradient modeling and computation of 3-D printed metamaterials for verifying constitutive parameters determined by asymptotic homogenization", pp. 343–357 in *Theoretical analyses, computations, and experiments of multiscale materials: a tribute to Francesco dell'Isola*, edited by I. Giorgio et al., Adv. Struct. Mater. **175**, Springer, 2022.

[7] E. Barchiesi, F. dell'Isola, and F. Hild, "On the validation of homogenized modeling for bi-pantographic metamaterials via digital image correlation", *Int. J. Solids Struct.* **208-209** (2021), 49–62.

[8] E. Barchiesi, A. Misra, L. Placidi, and E. Turco, "Granular micromechanics-based identification of isotropic strain gradient parameters for elastic geometrically nonlinear deformations", *ZAMM Z. Angew. Math. Mech.* **101**:11 (2021), art. id. e202100059.

[9] A. Casalotti and F. D'Annibale, "A rod-like piezoelectric controller for the improvement of the visco-elastic Beck's beam linear stability", *Struct. Control Health Monitor.* **29**:2 (2022), art. id. e2865.

[10] A. Casalotti, F. D'Annibale, and G. Rosi, "Multi-scale design of an architected composite structure with optimized graded properties", *Compos. Struct.* **252** (2020), art. id. 112608.

[11] N. Cefis, R. Fedele, and M. G. Beghi, "An integrated methodology to estimate the effective elastic parameters of amorphous TiO_2 nanostructured films, combining SEM images, finite element simulations and homogenization techniques", *Mech. Res. Commun.* **131** (2023), art. id. 104153.

[12] C. S. Chang and P.-Y. Hicher, "An elasto-plastic model for granular materials with microstructural consideration", *Int. J. Solids Struct.* **42**:14 (2005), 4258–4277.

[13] C. S. Chang, S. S. Sundaram, and A. Misra, "Initial moduli of particulated mass with frictional contacts", *Int. J. Numer. Anal. Meth. Geomech.* **13**:6 (1989), 629–644.

[14] A. Ciallella, F. D'Annibale, D. Del Vescovo, and I. Giorgio, "Deformation patterns in a second-gradient lattice annular plate composed of 'spira mirabilis' fibers", *Contin. Mech. Thermodyn.* **35**:4 (2023), 1561–1580.

[15] A. Ciallella, I. Giorgio, E. Barchiesi, et al., "A 3D pantographic metamaterial behaving as a mechanical shield: experimental and numerical evidence", *Mater. Design* **237** (2024), art. id. 112554.

[16] L. Contrafatto, M. Cuomo, and S. Gazzo, "A concrete homogenisation technique at meso-scale level accounting for damaging behaviour of cement paste and aggregates", *Comput. Struct.* **173** (2016), 1–18.

[17] P. A. Cundall and O. D. L. Strack, "A discrete numerical model for granular assemblies", *Géotechnique* **29**:1 (1979), 47–65.

[18] M. Cuomo, L. Contrafatto, and L. Greco, "A variational model based on isogeometric interpolation for the analysis of cracked bodies", *Int. J. Engrg. Sci.* **80** (2014), 173–188.

[19] M. Cuomo, F. dell'Isola, L. Greco, and N. L. Rizzi, "First versus second gradient energies for planar sheets with two families of inextensible fibres: investigation on deformation boundary layers, discontinuities and geometrical instabilities", *Compos. B* **115** (2017), 423–448.

[20] Y. F. Dafalias and M. T. Manzari, "Simple plasticity sand model accounting for fabric change effects", *J. Engrg. Mech.* **130**:6 (2004), 623–634.

[21] F. Darve (editor), *Geomaterials: constitutive equations and modelling*, CRC, London, 1990.

[22] M. De Angelo, N. Yilmaz, M. E. Yildizdag, A. Misra, F. Hild, and F. dell'Isola, "Identification and validation of constitutive parameters of a Hencky-type discrete model via experiments on millimetric pantographic unit cells", *Int. J. Non-Linear Mech.* **153** (2023), art. id. 104419.

[23] F. dell'Isola and A. Misra, "Principle of virtual work as foundational framework for metamaterial discovery and rational design", *Comptes Rendus. Mécanique* **351**:S3 (2023), 65–89.

[24] F. dell'Isola, U. Andreaus, and L. Placidi, "At the origins and in the vanguard of peridynamics, non-local and higher-gradient continuum mechanics: an underestimated and still topical contribution of Gabrio Piola", *Math. Mech. Solids* **20**:8 (2015), 887–928.

[25] F. dell'Isola, I. Giorgio, M. Pawlikowski, and N. L. Rizzi, "Large deformations of planar extensible beams and pantographic lattices: heuristic homogenization, experimental and numerical examples of equilibrium", *Proc. A* **472**:2185 (2016), art. id. 20150790.

[26] F. dell'Isola, M. Cuomo, L. Greco, and A. Della Corte, "Bias extension test for pantographic sheets: numerical simulations based on second gradient shear energies", *J. Engrg. Math.* **103** (2017), 127–157.

[27] F. dell'Isola, P. Seppecher, J. J. Alibert, et al., "Pantographic metamaterials: an example of mathematically driven design and of its technological challenges", *Contin. Mech. Thermodyn.* **31**:4 (2019), 851–884.

[28] N. Deng, A. Wautier, Y. Thiery, Z.-Y. Yin, P.-Y. Hicher, and F. Nicot, "On the attraction power of critical state in granular materials", *J. Mech. Phys. Solids* **149** (2021), art. id. 104300.

[29] V. A. Eremeyev, F. dell'Isola, C. Boutin, and D. Steigmann, "Linear pantographic sheets: existence and uniqueness of weak solutions", *J. Elasticity* **132**:2 (2018), 175–196.

[30] J. M. T. Espino, J. H. E. Sandoval, C. A. Tran, et al., "Validation of a hemi-variational block-based approach to the modelling of common in-plane failures in masonry structures", pp. 191–210 in *Sixty shades of generalized continua*, edited by H. Altenbach et al., Adv. Struct. Mater. **170**, Springer, 2023.

[31] S. R. Eugster, F. dell'Isola, R. Fedele, and P. Seppecher, "Piola transformations in second-gradient continua", *Mech. Res. Commun.* **120** (2022), art. id. 103836.

[32] F. Fabbrocino and G. Carpentieri, "Three-dimensional modeling of the wave dynamics of tensegrity lattices", *Compos. Struct.* **173** (2017), 9–16.

[33] F. Fabbrocino, M. F. Funari, F. Greco, P. Lonetti, R. Luciano, and R. Penna, "Dynamic crack growth based on moving mesh method", *Compos. B* **174** (2019), art. id. 107053.

[34] R. Fedele, G. Maier, and B. Miller, "Identification of elastic stiffness and local stresses in concrete dams by in situ tests and neural networks", *Struct. Infrastruct. Engrg.* **1**:3 (2005), 165–180.

[35] R. Fedele, A. Ciani, L. Galantucci, V. Casalegno, A. Ventrella, and M. Ferraris, "Characterization of innovative CFC/Cu joints by full-field measurements and finite elements", *Mater. Sci. Engrg. A* **595** (2014), 306–317.

[36] L. Feo, F. Greco, L. Leonetti, and R. Luciano, "Mixed-mode fracture in lightweight aggregate concrete by using a moving mesh approach within a multiscale framework", *Compos. Struct.* **123** (2015), 88–97.

[37] Z. Gao, J. Zhao, X.-S. Li, and Y. F. Dafalias, "A critical state sand plasticity model accounting for fabric evolution", *Int. J. Numer. Anal. Meth. Geomech.* **38**:4 (2014), 370–390.

[38] I. Giorgio, N. L. Rizzi, and E. Turco, "Continuum modelling of pantographic sheets for out-of-plane bifurcation and vibrational analysis", *Proc. A.* **473**:2207 (2017), art. id. 20170636.

[39] I. Giorgio, F. dell'Isola, and A. Misra, "Chirality in 2D Cosserat media related to stretch-micro-rotation coupling with links to granular micromechanics", *Int. J. Solids Struct.* **202** (2020), 28–38.

[40] I. Giorgio, F. Hild, E. Gerami, F. dell'Isola, and A. Misra, "Experimental verification of 2D Cosserat chirality with stretch-micro-rotation coupling in orthotropic metamaterials with granular motif", *Mech. Res. Commun.* **126** (2022), art. id. 104020.

[41] F. Greco, L. Leonetti, R. Luciano, and P. Trovalusci, "Multiscale failure analysis of periodic masonry structures with traditional and fiber-reinforced mortar joints", *Compos. B* **118** (2017), 75–95.

[42] L. Greco, M. Cuomo, and L. Contrafatto, "Two new triangular G^1-conforming finite elements with cubic edge rotation for the analysis of Kirchhoff plates", *Comput. Methods Appl. Mech. Engrg.* **356** (2019), 354–386.

[43] A. Grimaldi and R. Luciano, "Tensile stiffness and strength of fiber-reinforced concrete", *J. Mech. Phys. Solids* **48**:9 (2000), 1987–2008.

[44] P.-Y. Hicher and C. S. Chang, "A microstructural elastoplastic model for unsaturated granular materials", *Int. J. Solids Struct.* **4**:7-8 (2007), 2304–2323.

[45] K. L. Lee and H. B. Seed, "Drained strength characteristics of sands", *J. Soil Mech. Found. Divis.* **93**:6 (1967), 117–141.

[46] X. S. Li and Y. F. Dafalias, "Anisotropic critical state theory: role of fabric", *J. Engrg. Mech.* **138**:3 (2012), 263–275.

[47] S. Likitlersuang and G. T. Houlsby, "Development of hyperplasticity models for soil mechanics", *Int. J. Numer. Anal. Meth. Geomech.* **30**:3 (2006), 229–254.

[48] V. Maksimov, E. Barchiesi, A. Misra, L. Placidi, and D. Timofeev, "Two-dimensional analysis of size effects in strain-gradient granular solids with damage-induced anisotropy evolution", *J. Engrg. Mech.* **147**:11 (2021), 04021098.

[49] G. Mancusi, F. Fabbrocino, L. Feo, and F. Fraternali, "Size effect and dynamic properties of 2D lattice materials", *Compos. B* **112** (2017), 235–242.

[50] S. Masson and J. Martinez, "Micromechanical analysis of the shear behavior of a granular material", *J. Engrg. Mech.* **127**:10 (2001), 1007–1016.

[51] A. Misra and P. Poorsolhjouy, "Elastic behavior of 2D grain packing modeled as micromorphic media based on granular micromechanics", *J. Engrg. Mech.* **143**:1 (2017), art. id. C4016005.

[52] A. Misra, L. Placidi, and E. Turco, "Variational methods for discrete models of granular materials", pp. 2621–2634 in *Encyclopedia of continuum mechanics*, edited by H. Altenbach and A. Öchsner, Springer, 2020.

[53] A. A. Munjiza, *The combined finite-discrete element method*, Wiley, Chichester, 2004.

[54] N. Nejadsadeghi and A. Misra, "Extended granular micromechanics approach: a micromorphic theory of degree n", *Math. Mech. Solids* **25**:2 (2020), 407–429.

[55] N. Nejadsadeghi, F. Hild, and A. Misra, "Parametric experimentation to evaluate chiral bars representative of granular motif", *Int. J. Mech. Sci.* **221** (2022), art. id. 107184.

[56] T.-T. Ng, "Discrete element method simulations of the critical state of a granular material", *Int. J. Geomech.* **9**:5 (2009), 209–216.

[57] M. Nitka, G. Combe, C. Dascalu, and J. Desrues, "Two-scale modeling of granular materials: a DEM-FEM approach", *Granular Matter* **13**:3 (2011), 277–281.

[58] E. Oñate and J. Rojek, "Combination of discrete element and finite element methods for dynamic analysis of geomechanics problems", *Comput. Meth. Appl. Mech. Engrg.* **193**:27-29 (2004), 3087–3128.

[59] J.-h. Pan, G. Pinzón, R. Wang, E. Andò, G. Viggiani, and J.-M. Zhang, "Lessons learned from matching 3D DEM and experiments at macro, meso and fabric scales for triaxial compression tests on lentils", *J. Mech. Phys. Solids* **183** (2024), art. id. 105494.

[60] A. G. Papadimitriou, Y. K. Chaloulos, and Y. F. Dafalias, "A fabric-based sand plasticity model with reversal surfaces within anisotropic critical state theory", *Acta Geotech.* **14**:2 (2019), 253–277.

[61] L. Placidi, E. Barchiesi, A. Misra, and U. Andreaus, "Variational methods in continuum damage and fracture mechanics", pp. 2634–2643 in *Encyclopedia of continuum mechanics*, edited by H. Altenbach and A. Öchsner, Springer, 2020.

[62] L. Placidi, E. Barchiesi, A. Misra, and D. Timofeev, "Micromechanics-based elasto-plastic-damage energy formulation for strain gradient solids with granular microstructure", *Contin. Mech. Thermodyn.* **33**:5 (2021), 2213–2241.

[63] L. Placidi, D. Timofeev, V. Maksimov, E. Barchiesi, A. Ciallella, A. Misra, and F. dell'Isola, "Micro-mechano-morphology-informed continuum damage modeling with intrinsic 2nd gradient (pantographic) grain–grain interactions", *Int. J. Solids Struct.* **254-255** (2022), art. id. 111880.

[64] L. Placidi, E. Barchiesi, F. dell'Isola, V. Maksimov, A. Misra, N. Rezaei, A. Scrofani, and D. Timofeev, "On a hemi-variational formulation for a 2D elasto-plastic-damage strain gradient solid with granular microstructure", *Math. Eng.* **5**:1 (2023), art. id. 021.

[65] L. Placidi, F. dell'Isola, A. Kandalaft, R. Luciano, C. Majorana, and A. Misra, "A granular micromechanic-based model for ultra high performance fiber-reinforced concrete (UHP FRC)", *Int. J. Solids Struct.* **297** (2024), art. id. 112844.

[66] G. Ramaglia, G. P. Lignola, F. Fabbrocino, and A. Prota, "Numerical investigation of masonry strengthened with composites", *Polymers* **10**:3 (2018), art. id. 334.

[67] G. Ramaglia, F. Fabbrocino, G. P. Lignola, and A. Prota, "Impact of FRP and FRCM on the ductility of strengthened masonry members", *Structures* **28** (2020), 1229–1243.

[68] N. Rezaei, J. Riesselmann, A. Misra, D. Balzani, and L. Placidi, "A procedure for the experimental identification of the strain gradient characteristic length", *Z. Angew. Math. Phys.* **75**:3 (2024), art. id. 80.

[69] L. Rothenburg and N. P. Kruyt, "Critical state and evolution of coordination number in simulated granular materials", *Int. J. Solids Struct.* **41**:21 (2004), 5763–5774.

[70] M. Saberi, C.-D. Annan, J.-M. Konrad, and A. Lashkari, "A critical state two-surface plasticity model for gravelly soil-structure interfaces under monotonic and cyclic loading", *Comput. Geotech.* **80** (2016), 71–82.

[71] B. C. Sarar, M. E. Yildizdag, and B. E. Abali, "Comparison of homogenization techniques in strain gradient elasticity for determining material parameters", pp. 631–644 in *Sixty shades of generalized continua*, edited by H. Altenbach et al., Adv. Struct. Mater. **170**, Springer, 2023.

[72] B. C. Sarar, M. E. Yildizdag, and B. E. Abali, "A multi-scale homogenization framework for design and strain-gradient modeling of additively manufactured parts fabricated by particulate composites", *Contin. Mech. Thermodyn.* **36** (2024), 1629–1643.

[73] D. Sheng, S. W. Sloan, and H. S. Yu, "Aspects of finite element implementation of critical state models", *Computat. Mech.* **26** (2000), 185–196.

[74] L. Sibille, N. Hadda, F. Nicot, A. Tordesillas, and F. Darve, "Granular plasticity, a contribution from discrete mechanics", *J. Mech. Phys. Solids* **75** (2015), 119–139.

[75] S. F. Sizkow and U. El Shamy, "SPH-DEM simulations of saturated granular soils liquefaction incorporating particles of irregular shape", *Comput. Geotech.* **134** (2021), art. id. 104060.

[76] M. Spagnuolo, M. E. Yildizdag, X. Pinelli, A. Cazzani, and F. Hild, "Out-of-plane deformation reduction via inelastic hinges in fibrous metamaterials and simplified damage approach", *Math. Mech. Solids* **27**:6 (2022), 1011–1031.

[77] A. I. Theocharis, E. Vairaktaris, Y. F. Dafalias, and A. G. Papadimitriou, "Proof of incompleteness of critical state theory in granular mechanics and its remedy", *J. Engrg. Mech.* **143**:2 (2017), art. id. 04016117.

[78] A. I. Theocharis, E. Vairaktaris, Y. F. Dafalias, and A. G. Papadimitriou, "Necessary and sufficient conditions for reaching and maintaining critical state", *Int. J. Numer. Anal. Meth. Geomech.* **43**:12 (2019), 2041–2055.

[79] D. Timofeev, E. Barchiesi, A. Misra, and L. Placidi, "Hemivariational continuum approach for granular solids with damage-induced anisotropy evolution", *Math. Mech. Solids* **26**:5 (2021), 738–770.

[80] E. Turco, A. Misra, M. Pawlikowski, F. dell'Isola, and F. Hild, "Enhanced Piola–Hencky discrete models for pantographic sheets with pivots without deformation energy: numerics and experiments", *Int. J. Solids Struct.* **147** (2018), 94–109.

[81] E. Turco, F. dell'Isola, and A. Misra, "A nonlinear Lagrangian particle model for grains assemblies including grain relative rotations", *Int. J. Numer. Anal. Meth. Geomech.* **43**:5 (2019), 1051–1079.

[82] D. M. Wood, *Soil behaviour and critical state soil mechanics*, Cambridge Univ. Press, 1991.

[83] W. Wu, E. Bauer, and D. Kolymbas, "Hypoplastic constitutive model with critical state for granular materials", *Mech. Mater.* **23**:1 (1996), 45–69.

[84] W.-J. Xu, X.-Y. Dong, and W.-T. Ding, "Analysis of fluid-particle interaction in granular materials using coupled SPH-DEM method", *Powder Tech.* **353** (2019), 459–472.

[85] H. Yang, B. E. Abali, D. Timofeev, and W. H. Müller, "Determination of metamaterial parameters by means of a homogenization approach based on asymptotic analysis", *Contin. Mech. Thermodyn.* **32**:5 (2020), 1251–1270.

[86] M. E. Yildizdag, L. Placidi, and E. Turco, "Modeling and numerical investigation of damage behavior in pantographic layers using a hemivariational formulation adapted for a Hencky-type discrete model", *Continuum Mech. Thermodyn.* **35**:4 (2023), 1481–1494.

[87] M. E. Yildizdag, B. C. Sarar, A. Salvatori, G. D'Ovidio, and E. Turco, "Analysis of transmission and reflection characteristics of linear plane waves in pantographic lattices", *Z. Angew. Math. Phys.* **74**:5 (2023), art. id. 178.

[88] N. Yilmaz, M. E. Yildizdag, F. Fabbrocino, L. Placidi, and A. Misra, "Emergence of critical state in granular materials using a variationally-based damage-elasto-plastic micromechanical continuum model", *Int. J. Numer. Anal. Meth. Geomech.* **48**:13 (2024), 3369–3391.

[89] C.-F. Zhao, Z.-Y. Yin, A. Misra, and P.-Y. Hicher, "Thermomechanical formulation for micromechanical elasto-plasticity in granular materials", *Int. J. Solids Struct.* **138** (2018), 64–75.

[90] H. Zhu, H. N. G. Nguyen, F. Nicot, and F. Darve, "On a common critical state in localized and diffuse failure modes", *J. Mech. Phys. Solids* **95** (2016), 112–131.

Received 1 Oct 2024. Revised 11 Dec 2024. Accepted 20 Jan 2025.

NURETTIN YILMAZ: nurettin.yilmaz@graduate.univaq.it
International Research Center on Mathematics and Mechanics of Complex Systems University of L'Aquila, 67100 L'Aquila, Italy

LUCA PLACIDI: lplacidi@gmail.com
Faculty of Engineering, International Telematic University Uninettuno, 00186 Rome, Italy

ANIL MISRA: anmisra@fiu.edu
Department of Civil and Environmental Engineering, Florida International University, Miami, FL 33174, United States

FRANCESCO FABBROCINO: francesco.fabbrocino@unipegaso.it
Faculty of Engineering, International Telematic University Uninettuno, 00186 Rome, Italy